H2A.Z deposition at meiotic prophase I underlies homologous recombination and pachytene genome activation during male meiosis

Shenfei Sun[1,2,5,*], Yamei Jiang[2,5], Ning Jiang[2,5], Qiaoli Zhang[2], Hongjie Pan[3], Fujing Huang[2], Xinna Zhang[1], Yuxuan Guo[1], Xiaoyu You[2], Kai Gong[2], Wei Wei[2], Hanmin Liu[4], Zhenju Song[2], Yuanlin Song[2], Xiaofang Tang[2], Miao Yu[2], Runsheng Li[3], Xinhua Lin[1,2,4,6,*]

Affiliations

[1]State Key Laboratory of Reproductive Regulation and Breeding of Grassland Livestock, Institutes of Biomedical Sciences, School of Life Sciences, Inner Mongolia University, Hohhot 010070, China.

[2]State Key Laboratory of Genetic Engineering, Greater Bay Area Institute of Precision Medicine (Guangzhou), School of Life Sciences, Zhongshan Hospital, Fudan University, Shanghai 200438, China;

[3]National Health Commission (NHC) Key Laboratory of Reproduction Regulation, Shanghai Institute for Biomedical and Pharmaceutical Technologies, Shanghai 200032, China;

[4]The Joint Laboratory for Lung Development and Related Diseases of West China Second University Hospital, Sichuan University and School of Life Sciences of Fudan University, Chengdu 610041, China;

[5]These authors contributed equally to this work;

[6]Lead contact.

[*]Correspondence to: xlin@fudan.edu.cn (X.L.); shenfei_sun@fudan.edu.cn (S.S.).

Keywords: male meiosis; pachytene genome activation; homologous recombination; Znhit1; chromatin remodeling;

Abstract

Accurate meiotic progression is important for gamete formation and the generation of genetic diversity. However, little is known about the identity of chromatin regulators that underlie mammalian meiosis in vivo. Here, we identify the multifaceted functions of the chromatin remodeler Znhit1 in governing meiosis. We observe a gradual increase in *Znhit1* expression during the meiotic prophase. Znhit1 deficiency in spermatocytes results in arrested pachytene development, impaired DNA double-strand break repair, and defective homologous recombination. Single-cell RNA sequencing and transcriptome analysis reveal that Znhit1 loss downregulates the transcription of pachytene genome activation (PGA) genes globally. Chromatin immunoprecipitation data show that Znhit1 is needed for the incorporation of the histone variant H2A.Z into pachytene chromatin. Moreover, we find that H2A.Z cooperates with the transcription factor A-MYB to co-bind DNA elements and control enhancer activity. Our findings provide insights into the regulatory mechanisms governing meiotic progression and highlight Znhit1 as a critical regulator of meiotic recombination and PGA.

Introduction

Meiosis is a fundamental and conserved process that plays a crucial role in gamete formation and the generation of genetic diversity. By undergoing one round of DNA replication and two rounds of cell division, the meiotic process ensures the production of haploid cells, each with a unique combination of genetic materials (Handel and Schimenti, 2010; Lascarez-Lagunas et al., 2020). Any disruptions to the normal progression of meiosis would have significant consequences, such as aneuploidy, infertility, spontaneous abortion, and congenital diseases (Hassold and Hunt, 2001). Therefore, understanding the molecular mechanisms underlying meiosis will provide valuable insights for the diagnosis and treatment of reproductive and developmental diseases.

Multiple chromosomal events occur during meiotic prophase I, including homologous chromosome pairing and synapsis, DNA double-strand break (DSB) formation and repair, and homologous recombination (HR) (Baudat et al., 2013; Hunter, 2015; Zickler and Kleckner, 2023). In this process, homolog pairing and synapsis coincide with Spo11-mediated genome-wide formation of DSBs (Bergerat et al., 1997; Keeney et al., 1997). Following the formation of DSBs, the DNA undergoes resection, leading to the generation of single-stranded DNA overhangs. These overhangs are then coated by RPA, DMC1, and RAD51, facilitating the production of recombination intermediates. Subsequently, these intermediates are processed and resolved, ultimately forming either meiotic crossovers or non-crossovers (Gray and Cohen, 2016; San Filippo et al., 2008; Symington, 2014). The tightly coordinated timing and spatial arrangement of these meiotic events are of utmost importance for proper germ cell development.

There is transcriptional awakening during male meiotic prophase I, in which the quiescent meiotic genome becomes transcriptionally active during the zygotene-to-pachytene transition (Ernst et al., 2019; Green et al., 2018; Rabbani et al., 2022; Turner, 2015). This process, referred to as pachytene genome activation (PGA), is responsible for the expression of numerous genes and plays an essential role in controlling meiotic and post-meiotic events. Previous studies have emphasized the significance of the transcription factors (TFs) A-MYB, BRDT, and TCFL5 in activating transcription during pachytene (Alexander et al., 2023; Bolcun-Filas et al., 2011; Cecchini et al., 2023; Gaucher et al., 2012; Li et al., 2013; Maezawa et al., 2020; Manterola et al., 2018; Ozata et al., 2020; Yu et al., 2021). Additionally, extensive chromatin remodeling takes place in spermatocytes during meiotic prophase I, involving histone variant exchange, histone modifications, and high-order genome rearrangement (Kota and Feil, 2010; Wang et al., 2017; Zheng and

Xie, 2019). It has been known that SETDB1-mediated H3K9 trimethylation (H3K9me3) is required for sex chromosome transcription silencing (a process called meiotic sex chromosome inactivation, MSCI) and male meiotic procession (Hirota et al., 2018). However, the specific involvement of chromatin regulators in gene activation on autosomes remains poorly understood.

Zinc finger HIT-type containing 1 (Znhit1), an evolutionarily conserved subunit of the SRCAP chromatin remodeling complex, acts as a key regulator for the histone variant H2A.Z deposition to control gene expression and cell fate determination (Cai et al., 2005; Cuadrado et al., 2007; Feng et al., 2022). Recent studies have shown that Znhit1 is involved in a wide range of developmental processes, including muscle and lens differentiation, heart development, lung branching, and adult tissue stem cell maintenance (Cuadrado et al., 2010; Lu et al., 2022; Sun et al., 2020; Wei et al., 2022; Xu et al., 2021; Zhao et al., 2019). In our most recent study, we deleted Znhit1 in early male germ cells and found that Znhit1 is required for the mitosis-to-meiosis transition by controlling Meiosin expression (Sun et al., 2022). However, the in vivo function of Znhit1 in regulating meiotic progression remains unknown.

To delve into the function of Znhit1 in meiosis, we analyzed Znhit1 expression and observed upregulated Znhit1 expression specifically during meiotic prophase. Here, we examine the role of Znhit1 in multiple meiotic events and show that the deletion of Znhit1 in spermatocytes causes impaired HR and defective PGA, thereby resulting in meiotic developmental arrest. Hence, our study highlights the essential role of Znhit1 in ensuring meiotic progression, implicating its potential as a therapeutic target for meiosis-related diseases.

105 **Results**

106 ***Znhit1* expression is upregulated during meiotic prophase and *Znhit1* knockout in**
107 **spermatocytes disrupts spermatogenesis**

108 To identify potential chromatin regulators in meiosis, we first queried for chromatin
109 factors highly expressed during the zygotene stage based on published transcription data
110 (Fig S1A and Table S1) (Chen et al., 2018). Quantitative analysis showed that the
111 chromatin remodeler Znhit1 was among the most highly expressed factors (Figs 1A, 1B,
112 S1B, and S1C). RNA in situ hybridization validated that *Znhit1* expression in male germ
113 cells decreased after meiotic initiation, followed by a gradual increase in spermatocytes
114 from the zygotene stage to the metaphase stage (Fig 1C). These results suggest that
115 Znhit1 is a potential chromatin regulator of meiotic progression.

116 To investigate whether Znhit1 regulates meiotic progression, we generated spermatocyte-
117 specific *Znhit1* knockout mice (*Znhit1*$^{fl/fl}$; *Stra8-cre*, referred to as *Znhit1*-sKO). In the
118 first wave of spermatogenesis, Ngn3-negative prospermatogonia directly differentiate into
119 A2 spermatogonia(Law et al., 2019; Rabbani et al., 2022; Yoshida et al., 2006; Yoshida et
120 al., 2004). With Stra8-cre inducing recombination in A1 spermatogonia and preleptotene
121 spermatocytes separately(Lin et al., 2017), it is feasible to generate mice with
122 spermatocyte-specific gene knockout (Fig 1D). RNA in situ experiments on testis sections
123 confirmed *Znhit1* mRNA deletion in spermatocytes (Figs 1E and S1D). Compared with
124 littermate controls, *Znhit1*-sKO male mice had smaller testes (Fig S1E and S1F). PAS-
125 histological and PNA-fluorescence staining illuminated the absence of round spermatids
126 and elongated spermatids in *Znhit1*-sKO testes (Fig 1F and 1G), indicating that *Znhit1*
127 knockout in spermatocytes disrupted spermatogenesis.

128 **Znhit1 deletion leads to meiotic arrest at the pachytene stage**

129 To dissect spermatocyte development in *Znhit1*-sKO testes, we co-stained SYCP3, a
130 marker of primary spermatocytes, and HSPA2, a testis-specific HSP70 family member
131 that accumulates from the pachytene stage onward. As shown in Figure 2A, both control
132 and *Znhit1*-sKO testis sections exhibited SYCP3^{+}HSPA2^{+} primary spermatocytes.
133 Phospho-histone H3 (Thr3) (pH3) is a marker of mitotic and meiotic metaphase cells, and
134 Znhit1 deletion caused the complete absence of pH3^{+} metaphase spermatocytes within the
135 cavity of seminiferous tubules (Fig 2B). These results suggest that Znhit1 deletion causes
136 spermatocyte arrest at meiotic prophase I.

137 To pinpoint the onset of meiotic failure, we performed immunostaining against SYCP3 in
138 spermatocyte chromosome spreads. The wild-type testes displayed typical spermatocytes
139 at consecutive substages, including leptotene, zygotene, pachytene, diplotene, and
140 diakinesis (Fig 2C). However, spermatocytes at the diplotene and diakinesis stages were
141 rarely observed in *Znhit1*-sKO testes (Fig 2D and 2E). We also examined the expression
142 of H1T, a middle pachytene marker, and no difference in H1T expression was observed in
143 *Znhit1*$^{-/-}$ spermatocytes (Fig S2A). Moreover, *Znhit1* knockout resulted in increased
144 TUNEL-positive spermatocytes, suggesting that these defective spermatocytes were
145 eliminated by the apoptotic pathway (Fig 2F and 2G). These results indicate that Znhit1
146 deletion leads to meiotic arrest at the pachytene stage.

147 **Znhit1 is required for DSB repair and meiotic recombination**

148 To investigate the impact of Znhit1 on meiotic events, we first performed immunostaining
149 of SYCP1 and SYCP3, the essential components of the synaptonemal complex, to
150 examine whether Znhit1 regulated homologous synapses. As shown in Figure 3A,
151 pachytene nuclei with fully synapsed autosomes were observed in spermatocytes from
152 control and *Znhit1*-sKO testes. During the pachytene stage, the X and Y chromosomes
153 undergo pairing and synapses between the short pseudoautosomal regions (PARs). We
154 found an increase in the percentage of unsynapsed X-Y chromosomes in *Znhit1*-sKO
155 spermatocytes (Fig 3B). Thus, deletion of Znhit1 results in impaired sex chromosomal
156 synapsis.

157 Next, we examined the programmed formation and repair of DSBs by co-staining SYCP3
158 and γH2AX, a DSB marker, on spermatocyte chromosome spreads. In both control and
159 *Znhit1*-sKO spermatocytes, γH2AX signals were evident in the leptotene and zygotene
160 stages (Fig 3C). However, in Znhit1-deficient pachynema, we still observed diffuse
161 γH2AX signals on the autosomes, while in control pachynema, γH2AX signals only
162 accumulated on the X-Y chromosomes. Moreover, we detected the presence of another
163 DSB marker, phospho-ATM (pATM), on the autosomes in *Znhit1*-sKO pachytene
164 spermatocytes (Fig 3D). Together, these results demonstrate that Znhit1 is required for
165 completing DSB repair.

166 To understand how Znhit1 regulates DSB repair, we performed an immunostaining
167 analysis using the markers RPA2 and DMC1, the essential factors involved in DSB repair
168 by coating resected DSBs. We found an increase in RPA2 and DMC1 counts in both

169 zygonema and pachynema of *Znhit1*-deficient testes (Fig 3E, 3F, and S3A), indicating
170 that Znhit1 deletion delayed recombinational repair, resulting in defective resolution of
171 autosomal DSBs in *Znhit1*$^{-/-}$ pachynema. The formation and repair of DSBs play crucial
172 roles in initiating and facilitating meiotic recombination, respectively. To examine the
173 consequences of unrepaired DSBs on meiotic recombination in Znhit1 mutants, we
174 performed an immunostaining analysis against MLH1, a marker of meiotic crossover
175 formation. Indeed, we found an almost absence of MLH1 foci in *Znhit1*$^{-/-}$ pachytene
176 spermatocytes compared with controls (Fig 3G and 3H), indicating that the loss of Znhit1
177 severely disrupted meiotic crossover formation.

178 Collectively, these results argue that Znhit1 is essential for multiple meiotic events,
179 including sexual chromosome synapsis, DSB repair, and homologous recombination.

180 **scRNA-seq analysis reveals abnormal pachytene-to-diplotene transition caused by**
181 ***Znhit1* knockout**

182 We then asked how Znhit1 regulates spermatocyte development. We isolated testicular
183 cells from control and *Znhit1*-sKO mice at postnatal 16 (P16) and performed scRNA-seq
184 analysis. After quality control, a total of 2,4164 cells (12,212 cells from control, 11,952
185 cells from *Znhit1*-sKO) were captured, yielding 2,473 genes per cell. As visualized via
186 uniform manifold approximation and projection (UMAP), the single-cell atlas comprised
187 germ cells at various stages and major somatic cell types, including Sertoli cells (*Sox9*$^{+}$),
188 Leydig cells (*Hsd3b1*$^{+}$), peritubular myoid cells (*Acta2*$^{+}$), and macrophages (*Adgre1*$^{+}$)
189 (Figs 4A, 4B and S4A, and Table S2). The scRNA-seq data identified 6 germ cell types
190 based on the expression of specific markers, including undifferentiated spermatogonia
191 (*Zbtb16*$^{+}$), differentiating spermatogonia (*Kit*$^{+}$), preleptotene spermatocytes (*Nacad*$^{+}$),
192 leptotene spermatocytes (*Meiob*$^{+}$), zygotene spermatocytes (*Gml*$^{+}$), and pachytene
193 spermatocytes (*Ldhc*$^{+}$) (Fig 4B and 4C). Examination of germ cell scRNA-seq profiles
194 via unsupervised clustering revealed decreased pachytene spermatocytes after *Znhit1*
195 deletion (Figs 4D, 4E, and S4B). *Pou5f2* is expressed explicitly at the diplotene stage, and
196 we found a lack of *Pou5f2*$^{+}$ diplotene spermatocytes in *Znhit1*-sKO testes (Fig 4F). These
197 results indicate that Znhit1 is required for male germ cell development beyond the
198 pachytene stage.

199 **Znhit1 deletion impairs meiotic transcriptional activation**

200 Next, we asked whether meiotic transcriptional activation was affected by Znhit1
201 deletion. We analyzed changes in gene expression between consecutive spermatocyte
202 stages and identified 4,603 genes that showed significant changes (Fig 5A and Table S3).
203 Of the changed genes between zygotene spermatocytes and pachytene spermatocytes,
204 1,560 genes were upregulated (referred to as pachytene-activated genes or PGA genes).
205 Moreover, we identified differentially expressed genes (DEGs) in each spermatocyte type
206 between the control and *Znhit1*-sKO groups. The number of DEGs gradually increased
207 from the preleptotene stage to the pachytene stage, with downregulated genes being
208 predominant (Fig 5B and Table S4). In particular, *Znhit1*$^{-/-}$ pachytene spermatocytes
209 exhibited 2,785 downregulated genes, among which were most of the pachytene-activated
210 genes (1,094 out of 1,560, 70.1%; Figs 5B-5D, and S5A). Gene Ontology (GO)
211 enrichment analysis revealed that upregulated genes following Znhit1 deletion were
212 associated with apoptotic pathways, supporting an observation that Znhit1 deletion
213 resulted in germ cell clearance through apoptosis. Moreover, downregulated GO terms
214 included germ cell development and DNA recombination (Fig 5E and Table S5).
215 Interestingly, recent studies showed that cilium organization was essential for
216 spermatocyte development (Mytlis et al., 2022), and Znhit1 deletion reduced the
217 expression of cilium-related genes in zygotene and pachytene spermatocytes (Fig 5E).

218 We further conducted bulk RNA-seq experiments with P14 control and *Znhit1*-sKO
219 testicular cells and identified 882 DEGs (812 downregulated genes and 70 upregulated
220 genes) in *Znhit1*-sKO testicular cells (Figs 5F and S6A, and Table S6). Through
221 integrative analysis of bulk and single-cell RNA-seq data, we found that the expression of
222 these 812 genes was activated during the zygotene-to-pachytene transition and Znhit1
223 deletion significantly reduced the expression of these genes (Figs 5G, 5H, and S5B). The
224 downregulated genes following Znhit1 loss were enriched for germ cell-related GO terms,
225 such as cilium formation and spermatid development (Fig S6B). Together, these data
226 argue that Znhit1 is required for meiotic transcriptional activation.

227 Consistent with meiotic recombination defects in Znhit1 mutants, gene set enrichment
228 analysis (GSEA) revealed that the expression of HR-related genes was globally
229 downregulated following Znhit1 loss (Fig 5I and Table S7). The top genes associated
230 with this function included *Ccnb1ip1*, *Rnf212*, *Spo16*, *Ankrd31*, and *Terb1* (Boekhout et
231 al., 2019; Papanikos et al., 2019; Qiao et al., 2014; Rao et al., 2017; Reynolds et al., 2013;
232 Shibuya et al., 2014; Wang et al., 2019; Zhang et al., 2019) (Figs 5J, S6C, and S6D). As

233 expected, the Rnf212-dependent sumoylation level decreased in *Znhit1*$^{-/-}$ spermatocytes
234 (Fig 5K). These results suggest that Znhit1 regulates meiotic recombination by activating
235 HR-related genes.

236 **Znhit1 deletion impairs H2A.Z incorporation into pachytene chromatin**

237 We then asked how Znhit1 regulates transcription. Znhit1 is a subunit of the SRCAP
238 complex that facilitates the incorporation of the histone variant H2A.Z by replacing H2A
239 (Fig S7A). Immunostaining against H2A.Z showed a gradual increase in H2A.Z
240 accumulation on autosomes from the leptotene to the diakinesis stage, while the H2A.Z
241 signal was markedly low on the X-Y body (Fig 6A). Znhit1 loss decreased H2A.Z
242 staining on the pachytene cells, suggesting that Znhit1 is required for maintaining H2A.Z
243 integrity during meiosis.

244 To probe the H2A.Z targets, we performed chromatin immunoprecipitation followed by
245 sequencing (ChIP-seq) against H2A.Z in P14 testicular cells. Using the ChromHMM
246 model to annotate H2A.Z signals with meiocyte chromatin states defined by published
247 epigenetic markers (Spruce et al., 2020), we found that H2A.Z sites were primarily
248 enriched in chromatin state 1 and state 2 (promoters and enhancers) but were less
249 enriched in recombination hotspots (Fig 6B and 6C), consistent with previously published
250 results (Spruce et al., 2020). Quantitative analysis showed significant H2A.Z binding
251 reduction at 37.9% (23,926 of 63,109) of H2A.Z-bound genome sites following Znhit1
252 deletion (Fig 6D). Comparison analysis with bulk RNA-seq data identified 480
253 downregulated DEGs with decreased H2A.Z signals (Fig 6E). ~41.3 and 37.8% of the
254 downregulated H2A.Z peaks occupied promoters and enhancers, respectively. At
255 promoters, these downregulated H2A.Z preferentially occupied active promoters
256 (H3K4me3 only), while H2A.Z occupied three types of enhancers: active, poised, and
257 primed enhancers (Figs 6F, S7B, and S7C). These findings indicate that Znhit1 deletion
258 impairs H2A.Z incorporation into pachytene chromatin.

259 **H2A.Z deposition cooperates with A-MYB to regulate transcription**

260 We further asked how Znhit1/H2A.Z deposition facilitates lineage-specific gene
261 expression. We performed TF motif analysis using active promoters/enhancers with
262 decreased H2A.Z signals. This analysis identified several MYB family TFs, including
263 MYB, A-MYB, and B-MYB (Fig 7A). Transcriptional network analysis conducted by

264 SCENIC further identified A-MYB (encoded by *Mybl1* gene) as the core regulatory TF in
265 spermatocytes (Fig 7B). We reanalyzed RNA-seq data in P14 testes from A-MYB-
266 deficient mice (Li et al., 2013) and found that A-MYB-deficient DEGs correlated with
267 those observed in Znhit1-deficient testicular cells (Fig 7C). Although Znhit1 deletion
268 didn't affect *Mybl1* mRNA expression, transcriptome analyses showed that the expression
269 of A-MYB target genes was significantly reduced in *Znhit1*$^{-/-}$ pachytene spermatocytes
270 (Figs 7D, 7E, S8A, and S8B). These results suggest that *Znhit1*$^{-/-}$ and *Mybl1*$^{-/-}$ pachytene
271 spermatocytes share common gene expression alterations.

272 Next, we compared the genome binding sites of H2A.Z and A-MYB. Utilizing published
273 A-MYB ChIP-seq data from P14 testicular cells (Li et al., 2013), we identified 6,088 A-
274 MYB binding signals, with 78.1% (4755) of these coinciding with H2A.Z peaks (Fig 7F).
275 Annotation of genomic features showed that approximately 66.52% and 12.02% of these
276 overlapping sites occupied active promoters and enhancers, respectively, representing a
277 stronger enrichment compared to other regulatory elements (Fig 7G). Genes associated
278 with H2A.Z and A-MYB binding included essential HR-related genes, such as *Ccnb1ip1*
279 (encode the Hei10 protein) (Fig 7H). Moreover, we showed that Znhit1 deletion resulted
280 in a marked reduction in H2A.Z signals and nascent transcription identified by KAS-seq
281 signals (Fig 7I and 7J).

282 Previous studies have shown the fundamental role of A-MYB in activating meiotic
283 enhancers (Maezawa et al., 2020). Enhancer activity is linked to an increased formation
284 of enhancer single-stranded DNA (ssDNA), which can be evaluated using KAS-seq (Wu
285 et al., 2020). We found that the removal of Znhit1 resulted in abolished ssDNA at active
286 enhancers (Fig 7I and 7J). Interestingly, the chromatin accessibility detected by ATAC-
287 seq at active enhancers increased after Znhit1 deletion. These findings suggest that
288 Znhit1/H2A.Z deposition is essential for enhancer activation.

289 Together, these results demonstrate the critical role of the Znhit1/H2A.Z/A-MYB axis in
290 governing transcriptional activation and enhancer activity.
291

292 **Discussion**

293 Meiosis plays a crucial role in the production of haploid gametes. Any disturbances
294 during meiotic progress are known to lead to infertility and congenital diseases. Here we
295 delineate the multifaceted functions of the chromatin remodeler Znhit1 in regulating
296 meiotic progression. Our study provides convincing data to show that the
297 Znhit1/H2A.Z/A-MYB axis controls spermatocyte development, meiotic recombination,
298 and PGA. Thus, these findings underscore the significance of specific chromatin
299 structures in governing appropriate transcriptional reprogramming and precise meiotic
300 recombination.

301 The role of H2A.Z in DNA injury and repair has been extensively studied (Colino-
302 Sanguino et al., 2022; Dong et al., 2014; Xu et al., 2012; Yamada et al., 2018), but its
303 function in programmed DSB formation and repair during mammalian meiosis remains
304 unknown. To address this question, we generated Znhit1 conditional knockout mice
305 specifically during male meiosis to examine the role of Znhit1-mediated H2A.Z
306 deposition in the formation and repair of programmed DSB. One new observation in this
307 study is that Znhit1 loss is dispensable for DSB formation but necessary for DNA break
308 repair during meiosis. Intriguingly, unlike the observations in plant meiosis, we found that
309 H2A.Z does not directly bind DNA recombination sites in mammalian spermatocytes
310 (Choi et al., 2013; Spruce et al., 2020; Wang and Copenhaver, 2018). Moreover, we
311 showed that Znhit1 deletion delays recombinational repair, but has limited impacts on
312 DNA resection, ultimately causing defective meiotic crossover formation. Importantly,
313 our study demonstrates that Znhit1 is essential for the expression of meiotic
314 recombination-related genes, such as *Ccnb1ip1* and *Rnf212*, implying that Znhit1/H2A.Z
315 modulates meiotic recombination through transcriptional regulation. Therefore, our data
316 reveals a different mechanism underlying meiotic recombination between plants and
317 mammals.

318 Pachytene spermatocytes utilize a highly specific mechanism of meiotic surveillance, the
319 pachytene checkpoint, to prevent aneuploidy formation by removing abnormal germ cells
320 with incomplete chromosome synapsis and defective homologous recombination (Huang
321 and Roig, 2023; Roeder and Bailis, 2000; Subramanian and Hochwagen, 2014). Two
322 checkpoint pathways exist in male meiosis: one responding to unrepaired DSBs and the
323 other triggered by MSCI failure (Royo et al., 2013). However, whether epigenetic
324 regulation is involved in meiotic surveillance is not well defined. Previous studies have

325 reported that upon stimulation by unrepaired DSBs, the MRE11-ATM-CHK2 pathway is
326 activated to eliminate aberrant germ cells (Marcet-Ortega et al., 2017). Our study found
327 that Znhit1 deletion impairs the removal of ATM phosphorylation signals on autosomes
328 in pachynema, ultimately causing meiotic pachytene arrest and apoptosis. Therefore,
329 these findings demonstrate that Znhit1 acts as an important chromatin factor involved in
330 the regulation of the pachytene checkpoint.

331 It has long been noticed that in meiotic prophase I, chromatin that has not yet completed
332 chromosomal synapses is transcriptionally inactive, known as meiotic silencing of
333 unsynapsed chromatin (MSUC) (Turner et al., 2005). When germ cells enter the
334 pachytene stage, a large number of protein-coding genes and non-coding RNAs begin to
335 be actively expressed, known as PGA. Previous studies have shown that transcription
336 factors A-MYB and BRDT are involved in transcriptional activation during meiotic
337 prophase, but how PGA takes place in the chromatin context is unclear. In this study, we
338 found that the expression of the chromatin remodeler Znhit1 is specifically upregulated
339 during the zygotene-to-pachytene transition. We also observed that H2A.Z deposition is
340 enriched in the autosomes but less in the sex chromosome at the pachytene stage. Znhit1
341 deletion in spermatocytes repressed pachytene gene activation globally and reduced
342 chromosome-wide H2A.Z deposition, supporting a central role of Znhti1 in PGA
343 regulation and chromatin remodeling. It has been known that A-MYB is a transcription
344 factor that controls pachytene transcription activation. We found that Znhit1-deficient
345 spermatocytes phenocopied abnormal meiotic phenotypes in A-MYB mutants, such as X-
346 Y synapsis failure, impaired DSB repair, and defective HR (Alexander et al., 2023;
347 Bolcun-Filas et al., 2011; Li et al., 2013; Maezawa et al., 2020). Our results also revealed
348 that Znhit1/H2A.Z cooperates with A-MYB to regulate PGA gene activation. Therefore,
349 our study illuminates the molecular mechanisms underlying the fundamental question of
350 how PGA is regulated.

351 The histone variant H2A.Z is enriched at gene promoters and regulatory regions, but there
352 is ongoing debate regarding its involvement in transcriptional regulation. A recent paper
353 reported that H2A.Z knockout in post-mitotic muscle cells has limited effects on gene
354 expression (Belotti et al., 2020). In this study, we utilized the meiotic prophase as a model
355 system (where DNA replication does not occur) to study H2A.Z's function in
356 transcriptional regulation. We found that Znhit1-mediated H2A.Z deposition, independent
357 of DNA replication, is indispensable for the transcriptional activation of a large number

358 of meiotic genes. One explanation of this conflicting phenomenon is that H2A.Z
359 dynamics but not stable H2A.Z accumulation is essential for priming transcriptional
360 changes.

361 Through the integration of functional and molecular evidence, our findings establish the
362 critical involvement of Znhit1-dependent chromatin remodeling in the orchestration of
363 meiotic progression and coordination of various meiotic processes, such as HR and PGA.
364 Furthermore, we pinpoint the pivotal role played by the Znhit1/H2A.Z/A-MYB axis in
365 driving transcriptional reprogramming during meiotic prophase. Taken together, this
366 study deepens our understanding of the interplay between epigenetic regulation and
367 mammalian meiosis.

368 **Materials and Methods**

369 **Animals.** *Znhit1*$^{fl/fl}$ mice have been previously described (Zhao et al., 2019) and are
370 available from the Model Animal Research Center of Nanjing University (MARC,
371 Nanjing, China). The *Stra8-cre* knock-in mouse line was kindly provided by Dr. Ming-
372 Han Tong(Lin et al., 2017). All mice were maintained on the C57BL/6J background.
373 Germ cell-specific *Znhit1* knockout mice (*Znhit1*$^{fl/fl}$; *Stra8-cre*) were obtained by crossing
374 *Znhit1*$^{fl/+}$; *Stra8-cre* mice with *Znhit1*$^{fl/fl}$ mice. All mice were housed in the SPF (Specific-
375 Pathogen-Free) animal facility with standard 12 h light/dark cycles and standard
376 temperature (22 to 24°C). All mice were provided with ad libitum access to standard
377 laboratory food and water. All experiments in this study were performed following
378 relevant guidelines and approved by the Animal Care and Use Committee of Fudan
379 University.

380 **Histological and immunohistochemical analysis.** Testes were fixed in modified
381 Davidson's fixative as previously described (Latendresse et al., 2002), embedded in
382 paraffin, and sectioned. For periodic acid-Schiff (PAS)-hematoxylin staining, 5 μm testis
383 sections were deparaffinized, rehydrated, and stained with Schiff's reagent and
384 hematoxylin solution. For immunofluorescent staining, 5 μm testis sections were
385 retrieved by sodium citrate antigen retrieval buffer (pH 6.0) and blocked with 5% BSA in
386 PBS for 30 min at room temperature. The sections were later incubated overnight at 4°C
387 with primary antibodies as follows: mouse anti-SYCP3 (Abcam, ab97672), rabbit anti-
388 HSPA2 (Abcam, ab108416), rabbit anti-pH3 (Millipore, H0412), rabbit anti-H1T
389 (Invitrogen, PA5-51200), or lectin PNA (Sigma–Aldrich, L7381). On the following day,
390 secondary fluorescein-conjugated antibodies and DAPI (Sigma–Aldrich, D9542) were
391 added for 1 h, followed by Fluoromount-G mounting (Southern Biotech, 0100-01).
392 Images were analyzed using the confocal microscope.

393 TUNEL staining was carried out using the DeadEnd^{TM} Fluorometric TUNEL System
394 (Promega, G3250) according to the manufacturer's instructions.

395 **Immunostaining of spermatocyte chromosome spreads.** Spermatocyte chromosome
396 spreads were prepared as previously described (Alavattam et al., 2018). Briefly, the
397 clumps of seminiferous tubules were transferred to the hypotonic extraction buffer (30
398 mM Tris base, 17 mM trisodium citrate, 5 mM EDTA, 50 mM sucrose, 5 mM
399 dithiothreitol (DTT), and 1× protease inhibitor, pH 8.2) and incubated on ice for 1.5 h.
400 The clumps of tubules were then transferred to 30 μL of ice-cold 100 mM sucrose and
401 mashed gently using tweezers to obtain a cell suspension. An additional 30 μL of ice-cold
402 100 mM sucrose was added to the cell suspension and mixed several times. Positively
403 charged slides were incubated in the ice-cold fixation solution (2% paraformaldehyde,
404 0.1% Triton X-100, and 0.02% SDS, pH 9.2) for 3 min. 30 μL of the diluted cell
405 suspension was applied to the slides and incubated in humid chambers at room
406 temperature for 2 h. The slides were washed with 0.4% Photo-Flo 200 and stored at -
407 80°C.

408 For immunostaining of spermatocyte chromosome spreads, slides were washed with PBS
409 and blocked with 5% BSA in PBS for 30 min at room temperature. The slides were
410 stained with primary antibodies as follows: rabbit anti-SYCP3 (Abcam, ab15093), mouse
411 anti-SYCP3 (Abcam, ab97672), rabbit anti-SYCP1 (Abcam, ab15090), mouse anti-
412 γH2AX (BioLegend, 613401), rabbit anti-pATM (Millipore, 05-740), rabbit anti-RAD51
413 (Proteintech), rabbit anti-RPA2 (Proteintech, 10412-1-AP), rabbit anti-MLH1 (Cell
414 Signaling Technology, 3515T), rabbit anti-H2A.Z (Abcam, ab4174).

415 ***Znhit1* in situ hybridization.** Testis sections (5 μM) at the indicated times were prepared
416 for *Znhit1* in situ hybridization with the RNAscope kit (Advanced Cell Diagnostics,
417 323100) according to the manufacturer's instructions.

418 **Quantitative reverse transcription PCR (RT-qPCR).** Total RNA was isolated using the
419 RNeasy Mini-plus Kit (Qiagen, 74134) and then reverse-transcribed into complementary
420 DNA (cDNA) with the GoScript Reverse Transcription System (Promega, A5003). cDNA
421 was used as the template for the quantitative PCR assay using 2×SYBR Green qPCR
422 Master Mix (Bimake, B21202). Quantitative PCR primers are listed in Table S8.

423 **RNA-seq library generation and sequencing.** Total RNA from fresh testes was isolated
424 and mRNA was purified with magnetic beads (Vazyme, N401-01). Then, mRNA was
425 fragmented and processed to generate RNA-seq libraries (Vazyme, NR605-01). Over 40
426 million reads were obtained per sample using the Illumina NovaSeq platform for 2
427 independent biological replicates.

428 **Single-cell RNA sequencing (scRNA-seq).** P16 control and *Znhit1*-sKO testes were
429 digested by collagenase IV and trypsin at 37°C for 10 min to obtain testicular cell
430 suspensions. scRNA-seq libraries were constructed using a 10 × Genomics kit and
431 sequenced on the Illumina platform.

432 **ChIP-seq library generation and sequencing.** ChIP-seq library generation was
433 performed as previously described. Briefly, P14 control and *Znhit1*-sKO testes were
434 digested by collagenase IV and trypsin at 37°C for 10 min, crosslinked with 1%
435 formaldehyde for 10 min, and quenched with glycine. The cells were lysed and sheared
436 with a Bioruptor Plus machine for 20 min. Then, 2 μg of anti-H2A.Z antibody (Abcam,
437 ab4174) was added to the sonicated chromatin and incubated overnight at 4°C. The
438 following day, 20 μL of protein G beads were added and incubated for 2 h at 4°C. The
439 beads were washed and reverse-crosslinked for 4 h at 65°C. DNA was extracted using
440 phenol-chloroform and subjected to library construction using the VAHTS Universal
441 DNA Library Prep Kit for Illumina (Vazyme, ND607-01) according to the manufacturer's
442 instructions. Over 30 million reads were obtained per sample using the Illumina NovaSeq
443 platform for 2 independent biological replicates.

444 **KAS-seq library and ATAC-seq library generation and sequencing.** Testes were
445 digested by collagenase IV and trypsin at 37°C for 10 min. Pachytene cells were sorted
446 using fluorescence-activated cell sorting (FACS) as previously described (Long et al.,
447 2017). For KAS-seq, pachytene cells were labeled with N3-kethoxal, and DNA was
448 isolated using the DNA Clean and Concentrator kit (Zymo, D4013) and subjected to
449 library construction using Q5 high-fidelity DNA polymerase (New England Biolabs,
450 M0544S). Genomic DNA was fragmented using Tn5 transposase and subjected to library

451 construction. For ATAC-seq, pachytene nuclei were isolated and fragmented with Tn5
452 transposase. DNA was isolated using the DNA Clean and Concentrator kit (Zymo,
453 D4013) and subjected to library construction using Q5 high-fidelity DNA polymerase
454 (New England Biolabs, M0544S). For high-throughput sequencing, over 30 million reads
455 were obtained per sample using the Illumina NovaSeq platform for 2 independent
456 biological replicates.

457 **RNA-seq data analysis.** We performed RNA-seq analysis as described previously
458 (Pertea et al., 2016). Briefly, after removing adapters using Cutadapt (v2.5) (Kechin et al.,
459 2017), paired-end reads were aligned to the annotated mouse transcripts (mm10 Gencode
460 vM23 release) using Hisat2 (v2.2.1) (Kim et al., 2015; Kim et al., 2019). Gene expression
461 levels were calculated using StringTie (v2.2.1) (Pertea et al., 2015). Read counts were
462 calculated using a Python script (prepDE.py3) provided by the StringTie development
463 team. Differentially expressed genes were identified using the R package DESeq2
464 (v1.38.3) (Love et al., 2014). Genes with read counts > 50 in at least one sample were
465 kept for further analysis. A given gene was considered to significantly change if the
466 adjusted P value (padj) was < 0.05, the P value was < 0.01, and the fold-change was≥ 2.
467 Gene Set Enrichment Analysis (GSEA) was carried out using GSEA software
468 (Subramanian et al., 2005). GO analysis was performed using clusterProfiler (v4.6.2) (Wu
469 et al., 2021).

470 **scRNA-seq data analysis.** FASTQ files were run through CellRanger (v7.1.0) software
471 with default parameters for de-multiplexing, aligning reads with STAR software to
472 mm10, and counting unique molecular identifiers (UMIs). As input files of the Seurat R
473 package (v4.4.0), the filtered gene expression matrices were then used for downstream
474 analyses (Butler et al., 2018). Low-quality cells were filtered (expressing < 500 or >6,000
475 unique gene counts and >15% mitochondrial reads). Principal component analysis was
476 performed on SCT-transformed data using 3,000 variable genes. The top 50 principal
477 components were used for clustering and visualized using the UMAP algorithm in the
478 Seurat R package. The "FindAllMarkers" function of the Seurat R package was used to

479 calculate cluster-specific genes. Marker genes for each cluster are shown in Table S2.

480 The "FindMarkers" function of the Seurat R package was used to identify differentially
481 expressed genes (DEGs) for spermatocytes (preleptotene, leptotene, zygotene, and
482 pachytene). Only those with |'avg_logFC'| > 0.25 and 'p_val_adj' < 0.05 were considered
483 as DEGs. For the transcriptional regulatory network analysis, the raw count matrix was
484 used by the pyscenic (v0.12.1) workflow using default parameters (Aibar et al., 2017).
485 Then, the output loom file was opened by the SCENIC R package (v1.3.1), and AUC
486 values of regulons were extracted for visualization of downstream transcription factor
487 activity.

488 **ChIP-seq and KAS-seq data analysis.** For analyzing ChIP-seq and KAS-seq data, we
489 used the ENCODE ChIP-seq pipeline (v2.2.1, https://github.com/ENCODE-DCC/chip-
490 seq-pipeline2). Raw reads were cleaned by Cutadapt (v2.5) (Kechin et al., 2017). After
491 removing adapters, clean reads were aligned against the mouse mm10 genome using bwa
492 (v0.7.17) (Li and Durbin, 2009). Then, sam files were converted to bam files using
493 samtools (v1.9) (Li et al., 2009). PCR duplicates were removed using Picard (v2.20.7)
494 (https://broadinstitute.github.io/picard/). Histone ChIP-seq peaks (such as H2A.Z and
495 histone marks) and KAS-seq peaks were called using MACS2 (v2.2.4) (Zhang et al.,
496 2008), while transcription factor ChIP-seq peaks (such as A-Myb) were called using the R
497 packages spp (v1.15.5) (https://github.com/hms-dbmi/spp). The conservative narrow
498 peaks were used for downstream analysis.

499 For visualization, bam files were converted to bigWig files using deepTools (v3.3.1)
500 (Ramirez et al., 2014), and bigWig files were used to calculate tag density under 50 bp
501 resolution. In addition, CPM was used to normalize the number of reads per bin. We used
502 the R package DiffBind (v3.8.4)
503 (http://bioconductor.org/packages/release/bioc/html/DiffBind.html) for differential peak
504 analysis and the R package rGREAT (v2.1.11) (Gu and Hubschmann, 2023) for peak
505 annotation. We used ComputeMatrix and plotHeatmap of deepTools to generate count
506 matrices and heatmaps, respectively. H2A.Z enrichment within chromatin states was

507 annotated using the ChromHMM model (Ernst and Kellis, 2012; Spruce et al., 2020). TF
508 motif enrichment was calculated using HOMER (v4.11) (Heinz et al., 2010). We used
509 deepTools to draw Pearson's correlation scatter plots for the correlation between
510 replicates of each experiment.

511 For promoter and enhancer type analysis, H3K27ac ChIP-seq data in wild-type pachytene
512 spermatocytes were downloaded from the published data (GSE107398) (Adams et al.,
513 2018); ChIP-seq data for H3K4me1, H3K4me3, and H3K27me3 in wild-type pachytene
514 spermatocytes were downloaded from the published data (GSE132446) (Chen et al.,
515 2020).

516 **ATAC-seq data analysis.** ATAC-seq data were analyzed using a standardized ENCODE
517 ATAC-seq pipeline (v2.2.2, https://github.com/ENCODE-DCC/atac-seq-pipeline). The
518 mouse reference genome (mm10) was used in the pipeline. Trimming, mapping, and
519 duplicate-removing were performed as the ENCODE pipeline suggested using Cutadapt
520 (v2.5) (Kechin et al., 2017), Bowtie2 (v2.3.4.3) (Langmead et al., 2009), and Picard
521 (v2.20.7) (https://broadinstitute.github.io/picard/) respectively. MACS2 (v2.2.4) (Zhang
522 et al., 2008) was used for peak calling.

523 **Statistics and reproducibility.** Statistical analyses were performed using R and Prism 9.
524 Data are presented as means ± s.d. unless otherwise indicated. The two-tailed, unpaired,
525 Student's t-test, Mann–Whitney test, or one-way or two-way ANOVA were performed to
526 analyze statistical significance.

527 **Supplementary Materials**

528 This manuscript file includes Figs. S1 to S9 and Tables S1 and S8.
529

530 **Reference**

531 Adams, S.R., Maezawa, S., Alavattam, K.G., Abe, H., Sakashita, A., Shroder, M., Broering, T.J.,
532 Sroga Rios, J., Thomas, M.A., Lin, X.*, et al.* (2018). RNF8 and SCML2 cooperate to regulate
533 ubiquitination and H3K27 acetylation for escape gene activation on the sex chromosomes. PLoS
534 genetics *14*, e1007233.
535 Aibar, S., Gonzalez-Blas, C.B., Moerman, T., Huynh-Thu, V.A., Imrichova, H., Hulselmans, G.,
536 Rambow, F., Marine, J.C., Geurts, P., Aerts, J.*, et al.* (2017). SCENIC: single-cell regulatory network
537 inference and clustering. Nature methods *14*, 1083-1086.
538 Alavattam, K.G., Abe, H., Sakashita, A., and Namekawa, S.H. (2018). Chromosome Spread
539 Analyses of Meiotic Sex Chromosome Inactivation. Methods in molecular biology (Clifton, NJ)
540 *1861*, 113-129.
541 Alexander, A.K., Rice, E.J., Lujic, J., Simon, L.E., Tanis, S., Barshad, G., Zhu, L., Lama, J., Cohen, P.E.,
542 and Danko, C.G. (2023). A-MYB and BRDT-dependent RNA Polymerase II pause release
543 orchestrates transcriptional regulation in mammalian meiosis. Nature communications *14*.
544 Baudat, F., Imai, Y., and de Massy, B. (2013). Meiotic recombination in mammals: localization and
545 regulation. Nature reviews Genetics *14*, 794-806.
546 Belotti, E., Lacoste, N., Simonet, T., Papin, C., Padmanabhan, K., Scionti, I., Gangloff, Y.G., Ramos,
547 L., Dalkara, D., Hamiche, A.*, et al.* (2020). H2A.Z is dispensable for both basal and activated
548 transcription in post-mitotic mouse muscles. Nucleic acids research *48*, 4601-4613.
549 Bergerat, A., de Massy, B., Gadelle, D., Varoutas, P.C., Nicolas, A., and Forterre, P. (1997). An
550 atypical topoisomerase II from Archaea with implications for meiotic recombination. Nature *386*,
551 414-417.
552 Boekhout, M., Karasu, M.E., Wang, J., Acquaviva, L., Pratto, F., Brick, K., Eng, D.Y., Xu, J., Camerini-
553 Otero, R.D., Patel, D.J.*, et al.* (2019). REC114 Partner ANKRD31 Controls Number, Timing, and
554 Location of Meiotic DNA Breaks. Molecular cell *74*, 1053-1068 e1058.
555 Bolcun-Filas, E., Bannister, L.A., Barash, A., Schimenti, K.J., Hartford, S.A., Eppig, J.J., Handel, M.A.,
556 Shen, L., and Schimenti, J.C. (2011). A-MYB (MYBL1) transcription factor is a master regulator of
557 male meiosis. Development *138*, 3319-3330.
558 Butler, A., Hoffman, P., Smibert, P., Papalexi, E., and Satija, R. (2018). Integrating single-cell
559 transcriptomic data across different conditions, technologies, and species. Nature biotechnology
560 *36*, 411-420.
561 Cai, Y., Jin, J., Florens, L., Swanson, S.K., Kusch, T., Li, B., Workman, J.L., Washburn, M.P., Conaway,
562 R.C., and Conaway, J.W. (2005). The mammalian YL1 protein is a shared subunit of the
563 TRRAP/TIP60 histone acetyltransferase and SRCAP complexes. The Journal of biological
564 chemistry *280*, 13665-13670.
565 Cecchini, K., Biasini, A., Yu, T., Saflund, M., Mou, H., Arif, A., Eghbali, A., Colpan, C., Gainetdinov, I.,
566 de Rooij, D.G.*, et al.* (2023). The transcription factor TCFL5 responds to A-MYB to elaborate the
567 male meiotic program in mice. Reproduction *165*, 183-196.
568 Chen, Y., Lyu, R.T., Rong, B.W., Zheng, Y.X., Lin, Z., Dai, R.F., Zhang, X., Xie, N.N., Wang, S.Q.,
569 Tang, F.C.*, et al.* (2020). Refined spatial temporal epigenomic profiling reveals intrinsic
570 connection between PRDM9-mediated H3K4me3 and the fate of double-stranded breaks. Cell
571 research *30*, 256-268.
572 Chen, Y., Zheng, Y., Gao, Y., Lin, Z., Yang, S., Wang, T., Wang, Q., Xie, N., Hua, R., Liu, M.*, et al.*
573 (2018). Single-cell RNA-seq uncovers dynamic processes and critical regulators in mouse

spermatogenesis. Cell research *28*, 879-896.
Choi, K., Zhao, X., Kelly, K.A., Venn, O., Higgins, J.D., Yelina, N.E., Hardcastle, T.J., Ziolkowski, P.A., Copenhaver, G.P., Franklin, F.C.*, et al.* (2013). Arabidopsis meiotic crossover hot spots overlap with H2A.Z nucleosomes at gene promoters. Nature genetics *45*, 1327-1336.
Colino-Sanguino, Y., Clark, S.J., and Valdes-Mora, F. (2022). The H2A.Z-nuclesome code in mammals: emerging functions. Trends in genetics : TIG *38*, 273-289.
Cuadrado, A., Corrado, N., Perdiguero, E., Lafarga, V., Munoz-Canoves, P., and Nebreda, A.R. (2010). Essential role of p18Hamlet/SRCAP-mediated histone H2A.Z chromatin incorporation in muscle differentiation. The EMBO journal *29*, 2014-2025.
Cuadrado, A., Lafarga, V., Cheung, P.C., Dolado, I., Llanos, S., Cohen, P., and Nebreda, A.R. (2007). A new p38 MAP kinase-regulated transcriptional coactivator that stimulates p53-dependent apoptosis. The EMBO journal *26*, 2115-2126.
Dong, S., Han, J., Chen, H., Liu, T., Huen, M.S., Yang, Y., Guo, C., and Huang, J. (2014). The Human SRCAP Chromatin Remodeling Complex Promotes DNA-End Resection. Current biology : CB *24*, 2097-2110.
Ernst, C., Eling, N., Martinez-Jimenez, C.P., Marioni, J.C., and Odom, D.T. (2019). Staged developmental mapping and X chromosome transcriptional dynamics during mouse spermatogenesis. Nature communications *10*, 1251.
Ernst, J., and Kellis, M. (2012). ChromHMM: automating chromatin-state discovery and characterization. Nature methods *9*, 215-216.
Feng, Y., Zhang, Y., Lin, Z., Ye, X., Lin, X., Lv, L., Lin, Y., Sun, S., Qi, Y., and Lin, X. (2022). Chromatin remodeler Dmp18 regulates apoptosis by controlling H2Av incorporation in Drosophila imaginal disc development. PLoS genetics *18*, e1010395.
Gaucher, J., Boussouar, F., Montellier, E., Curtet, S., Buchou, T., Bertrand, S., Hery, P., Jounier, S., Depaux, A., Vitte, A.L.*, et al.* (2012). Bromodomain-dependent stage-specific male genome programming by Brdt. The EMBO journal *31*, 3809-3820.
Gray, S., and Cohen, P.E. (2016). Control of Meiotic Crossovers: From Double-Strand Break Formation to Designation. Annu Rev Genet *50*, 175-210.
Green, C.D., Ma, Q., Manske, G.L., Shami, A.N., Zheng, X., Marini, S., Moritz, L., Sultan, C., Gurczynski, S.J., Moore, B.B.*, et al.* (2018). A Comprehensive Roadmap of Murine Spermatogenesis Defined by Single-Cell RNA-Seq. Developmental cell *46*, 651-667 e610.
Gu, Z., and Hubschmann, D. (2023). rGREAT: an R/bioconductor package for functional enrichment on genomic regions. Bioinformatics *39*.
Handel, M.A., and Schimenti, J.C. (2010). Genetics of mammalian meiosis: regulation, dynamics and impact on fertility. Nature reviews Genetics *11*, 124-136.
Hassold, T., and Hunt, P. (2001). To err (meiotically) is human: the genesis of human aneuploidy. Nature reviews Genetics *2*, 280-291.
Heinz, S., Benner, C., Spann, N., Bertolino, E., Lin, Y.C., Laslo, P., Cheng, J.X., Murre, C., Singh, H., and Glass, C.K. (2010). Simple combinations of lineage-determining transcription factors prime cis-regulatory elements required for macrophage and B cell identities. Molecular cell *38*, 576-589.
Hirota, T., Blakeley, P., Sangrithi, M.N., Mahadevaiah, S.K., Encheva, V., Snijders, A.P., Ellnati, E., Ojarikre, O.A., de Rooij, D.G., Niakan, K.K.*, et al.* (2018). SETDB1 Links the Meiotic DNA Damage Response to Sex Chromosome Silencing in Mice. Developmental cell *47*, 645-+.

618 Huang, Y., and Roig, I. (2023). Genetic control of meiosis surveillance mechanisms in mammals.
619 Front Cell Dev Biol *11*, 1127440.
620 Hunter, N. (2015). Meiotic Recombination: The Essence of Heredity. Cold Spring Harbor
621 perspectives in biology *7*.
622 Kechin, A., Boyarskikh, U., Kel, A., and Filipenko, M. (2017). cutPrimers: A New Tool for Accurate
623 Cutting of Primers from Reads of Targeted Next Generation Sequencing. J Comput Biol *24*,
624 1138-1143.
625 Keeney, S., Giroux, C.N., and Kleckner, N. (1997). Meiosis-specific DNA double-strand breaks are
626 catalyzed by Spo11, a member of a widely conserved protein family. Cell *88*, 375-384.
627 Kim, D., Langmead, B., and Salzberg, S.L. (2015). HISAT: a fast spliced aligner with low memory
628 requirements. Nature methods *12*, 357-360.
629 Kim, D., Paggi, J.M., Park, C., Bennett, C., and Salzberg, S.L. (2019). Graph-based genome
630 alignment and genotyping with HISAT2 and HISAT-genotype. Nature biotechnology *37*, 907-
631 915.
632 Kota, S.K., and Feil, R. (2010). Epigenetic transitions in germ cell development and meiosis.
633 Developmental cell *19*, 675-686.
634 Langmead, B., Trapnell, C., Pop, M., and Salzberg, S.L. (2009). Ultrafast and memory-efficient
635 alignment of short DNA sequences to the human genome. Genome biology *10*, R25.
636 Lascarez-Lagunas, L., Martinez-Garcia, M., and Colaiacovo, M. (2020). SnapShot: Meiosis -
637 Prophase I. Cell *181*, 1442-1442 e1441.
638 Latendresse, J.R., Warbrittion, A.R., Jonassen, H., and Creasy, D.M. (2002). Fixation of testes and
639 eyes using a modified Davidson's fluid: comparison with Bouin's fluid and conventional
640 Davidson's fluid. Toxicol Pathol *30*, 524-533.
641 Law, N.C., Oatley, M.J., and Oatley, J.M. (2019). Developmental kinetics and transcriptome
642 dynamics of stem cell specification in the spermatogenic lineage. Nature communications *10*,
643 2787.
644 Li, H., and Durbin, R. (2009). Fast and accurate short read alignment with Burrows-Wheeler
645 transform. Bioinformatics *25*, 1754-1760.
646 Li, H., Handsaker, B., Wysoker, A., Fennell, T., Ruan, J., Homer, N., Marth, G., Abecasis, G., Durbin,
647 R., and Genome Project Data Processing, S. (2009). The Sequence Alignment/Map format and
648 SAMtools. Bioinformatics *25*, 2078-2079.
649 Li, X.Z., Roy, C.K., Dong, X., Bolcun-Filas, E., Wang, J., Han, B.W., Xu, J., Moore, M.J., Schimenti,
650 J.C., Weng, Z.*, et al.* (2013). An ancient transcription factor initiates the burst of piRNA production
651 during early meiosis in mouse testes. Molecular cell *50*, 67-81.
652 Lin, Z., Hsu, P.J., Xing, X., Fang, J., Lu, Z., Zou, Q., Zhang, K.J., Zhang, X., Zhou, Y., Zhang, T.*, et al.*
653 (2017). Mettl3-/Mettl14-mediated mRNA N6-methyladenosine modulates murine
654 spermatogenesis. Cell research.
655 Long, J., Huang, C., Chen, Y., Zhang, Y., Shi, S., Wu, L., Liu, Y., Liu, C., Wu, J., and Lei, M. (2017).
656 Telomeric TERB1-TRF1 interaction is crucial for male meiosis. Nat Struct Mol Biol *24*, 1073-1080.
657 Love, M.I., Huber, W., and Anders, S. (2014). Moderated estimation of fold change and dispersion
658 for RNA-seq data with DESeq2. Genome biology *15*, 550.
659 Lu, J., An, J., Wang, J., Cao, X., Cao, Y., Huang, C., Jiao, S., Yan, D., Lin, X., and Zhou, X. (2022).
660 Znhit1 Regulates p21Cip1 to Control Mouse Lens Differentiation. Investigative ophthalmology &
661 visual science *63*, 18.

662 Maezawa, S., Sakashita, A., Yukawa, M., Chen, X., Takahashi, K., Alavattam, K.G., Nakata, I.,
663 Weirauch, M.T., Barski, A., and Namekawa, S.H. (2020). Super-enhancer switching drives a burst
664 in gene expression at the mitosis-to-meiosis transition. Nat Struct Mol Biol *27*, 978-988.
665 Manterola, M., Brown, T.M., Oh, M.Y., Garyn, C., Gonzalez, B.J., and Wolgemuth, D.J. (2018). BRDT
666 is an essential epigenetic regulator for proper chromatin organization, silencing of sex
667 chromosomes and crossover formation in male meiosis. PLoS genetics *14*, e1007209.
668 Marcet-Ortega, M., Pacheco, S., Martinez-Marchal, A., Castillo, H., Flores, E., Jasin, M., Keeney, S.,
669 and Roig, I. (2017). p53 and TAp63 participate in the recombination-dependent pachytene arrest
670 in mouse spermatocytes. PLoS genetics *13*, e1006845.
671 Mytlis, A., Kumar, V., Qiu, T., Deis, R., Hart, N., Levy, K., Masek, M., Shawahny, A., Ahmad, A., Eitan,
672 H.*, et al.* (2022). Control of meiotic chromosomal bouquet and germ cell morphogenesis by the
673 zygotene cilium. Science, eabh3104.
674 Ozata, D.M., Yu, T., Mou, H., Gainetdinov, I., Colpan, C., Cecchini, K., Kaymaz, Y., Wu, P.H., Fan, K.,
675 Kucukural, A.*, et al.* (2020). Evolutionarily conserved pachytene piRNA loci are highly divergent
676 among modern humans. Nat Ecol Evol *4*, 156-168.
677 Papanikos, F., Clement, J.A.J., Testa, E., Ravindranathan, R., Grey, C., Dereli, I., Bondarieva, A.,
678 Valerio-Cabrera, S., Stanzione, M., Schleiffer, A.*, et al.* (2019). Mouse ANKRD31 Regulates
679 Spatiotemporal Patterning of Meiotic Recombination Initiation and Ensures Recombination
680 between X and Y Sex Chromosomes. Molecular cell *74*, 1069-1085 e1011.
681 Pertea, M., Kim, D., Pertea, G.M., Leek, J.T., and Salzberg, S.L. (2016). Transcript-level expression
682 analysis of RNA-seq experiments with HISAT, StringTie and Ballgown. Nature protocols *11*,
683 1650-1667.
684 Pertea, M., Pertea, G.M., Antonescu, C.M., Chang, T.C., Mendell, J.T., and Salzberg, S.L. (2015).
685 StringTie enables improved reconstruction of a transcriptome from RNA-seq reads. Nature
686 biotechnology *33*, 290-295.
687 Qiao, H., Prasada Rao, H.B., Yang, Y., Fong, J.H., Cloutier, J.M., Deacon, D.C., Nagel, K.E., Swartz,
688 R.K., Strong, E., Holloway, J.K.*, et al.* (2014). Antagonistic roles of ubiquitin ligase HEI10 and
689 SUMO ligase RNF212 regulate meiotic recombination. Nature genetics *46*, 194-199.
690 Rabbani, M., Zheng, X., Manske, G.L., Vargo, A., Shami, A.N., Li, J.Z., and Hammoud, S.S. (2022).
691 Decoding the Spermatogenesis Program: New Insights from Transcriptomic Analyses. Annu Rev
692 Genet *56*, 339-368.
693 Ramirez, F., Dundar, F., Diehl, S., Gruning, B.A., and Manke, T. (2014). deepTools: a flexible
694 platform for exploring deep-sequencing data. Nucleic acids research *42*, W187-191.
695 Rao, H.B., Qiao, H., Bhatt, S.K., Bailey, L.R., Tran, H.D., Bourne, S.L., Qiu, W., Deshpande, A.,
696 Sharma, A.N., Beebout, C.J.*, et al.* (2017). A SUMO-ubiquitin relay recruits proteasomes to
697 chromosome axes to regulate meiotic recombination. Science *355*, 403-407.
698 Reynolds, A., Qiao, H.Y., Yang, Y., Chen, J.K., Jackson, N., Biswas, K., Holloway, J.K., Baudat, F., de
699 Massy, B., Wang, J.*, et al.* (2013). RNF212 is a dosage-sensitive regulator of crossing-over during
700 mammalian meiosis. Nature genetics *45*, 269-278.
701 Roeder, G.S., and Bailis, J.M. (2000). The pachytene checkpoint. Trends in genetics : TIG *16*, 395-
702 403.
703 Royo, H., Prosser, H., Ruzankina, Y., Mahadevaiah, S.K., Cloutier, J.M., Baumann, M., Fukuda, T.,
704 Hoog, C., Toth, A., de Rooij, D.G.*, et al.* (2013). ATR acts stage specifically to regulate multiple
705 aspects of mammalian meiotic silencing. Genes & development *27*, 1484-1494.

San Filippo, J., Sung, P., and Klein, H. (2008). Mechanism of eukaryotic homologous recombination. Annual review of biochemistry *77*, 229-257.

Shibuya, H., Ishiguro, K., and Watanabe, Y. (2014). The TRF1-binding protein TERB1 promotes chromosome movement and telomere rigidity in meiosis. Nature cell biology *16*, 145-156.

Spruce, C., Dlamini, S., Ananda, G., Bronkema, N., Tian, H., Paigen, K., Carter, G.W., and Baker, C.L. (2020). HELLS and PRDM9 form a pioneer complex to open chromatin at meiotic recombination hot spots. Genes & development *34*, 398-412.

Subramanian, A., Tamayo, P., Mootha, V.K., Mukherjee, S., Ebert, B.L., Gillette, M.A., Paulovich, A., Pomeroy, S.L., Golub, T.R., Lander, E.S.*, et al.* (2005). Gene set enrichment analysis: a knowledge-based approach for interpreting genome-wide expression profiles. Proceedings of the National Academy of Sciences of the United States of America *102*, 15545-15550.

Subramanian, V.V., and Hochwagen, A. (2014). The meiotic checkpoint network: step-by-step through meiotic prophase. Cold Spring Harbor perspectives in biology *6*, a016675.

Sun, S., Jiang, N., Jiang, Y., He, Q., He, H., Wang, X., Yang, L., Li, R., Liu, F., Lin, X.*, et al.* (2020). Chromatin remodeler Znhit1 preserves hematopoietic stem cell quiescence by determining the accessibility of distal enhancers. Leukemia *34*, 3348-3358.

Sun, S., Jiang, Y., Zhang, Q., Pan, H., Li, X., Yang, L., Huang, M., Wei, W., Wang, X., Qiu, M.*, et al.* (2022). Znhit1 controls meiotic initiation in male germ cells by coordinating with Stra8 to activate meiotic gene expression. Developmental cell *57*, 901-913 e904.

Symington, L.S. (2014). End resection at double-strand breaks: mechanism and regulation. Cold Spring Harbor perspectives in biology *6*.

Turner, J.M. (2015). Meiotic Silencing in Mammals. Annu Rev Genet *49*, 395-412.

Turner, J.M., Mahadevaiah, S.K., Fernandez-Capetillo, O., Nussenzweig, A., Xu, X., Deng, C.X., and Burgoyne, P.S. (2005). Silencing of unsynapsed meiotic chromosomes in the mouse. Nature genetics *37*, 41-47.

Wang, L., Xu, Z., Khawar, M.B., Liu, C., and Li, W. (2017). The histone codes for meiosis. Reproduction *154*, R65-R79.

Wang, Y., Chen, Y., Chen, J., Wang, L., Nie, L., Long, J., Chang, H., Wu, J., Huang, C., and Lei, M. (2019). The meiotic TERB1-TERB2-MAJIN complex tethers telomeres to the nuclear envelope. Nature communications *10*, 564.

Wang, Y., and Copenhaver, G.P. (2018). Meiotic Recombination: Mixing It Up in Plants. Annu Rev Plant Biol *69*, 577-609.

Wei, W., Tang, X., Jiang, N., Ni, C., He, H., Sun, S., Yu, M., Yu, C., Qiu, M., Yan, D.*, et al.* (2022). Chromatin remodeler Znhit1 controls bone morphogenetic protein signaling in embryonic lung tissue branching. The Journal of biological chemistry *298*, 102490.

Wu, T., Hu, E., Xu, S., Chen, M., Guo, P., Dai, Z., Feng, T., Zhou, L., Tang, W., Zhan, L.*, et al.* (2021). clusterProfiler 4.0: A universal enrichment tool for interpreting omics data. Innovation (Camb) *2*, 100141.

Wu, T., Lyu, R., You, Q., and He, C. (2020). Kethoxal-assisted single-stranded DNA sequencing captures global transcription dynamics and enhancer activity in situ. Nature methods *17*, 515-523.

Xu, M., Yao, J., Shi, Y., Yi, H., Zhao, W., Lin, X., and Yang, Z. (2021). The SRCAP chromatin remodeling complex promotes oxidative metabolism during prenatal heart development. Development *148*.

750 Xu, Y., Ayrapetov, M.K., Xu, C., Gursoy-Yuzugullu, O., Hu, Y., and Price, B.D. (2012). Histone
751 H2A.Z controls a critical chromatin remodeling step required for DNA double-strand break
752 repair. Molecular cell *48*, 723-733.
753 Yamada, S., Kugou, K., Ding, D.Q., Fujita, Y., Hiraoka, Y., Murakami, H., Ohta, K., and Yamada, T.
754 (2018). The histone variant H2A.Z promotes initiation of meiotic recombination in fission yeast.
755 Nucleic acids research *46*, 609-620.
756 Yoshida, S., Sukeno, M., Nakagawa, T., Ohbo, K., Nagamatsu, G., Suda, T., and Nabeshima, Y.
757 (2006). The first round of mouse spermatogenesis is a distinctive program that lacks the self-
758 renewing spermatogonia stage. Development *133*, 1495-1505.
759 Yoshida, S., Takakura, A., Ohbo, K., Abe, K., Wakabayashi, J., Yamamoto, M., Suda, T., and
760 Nabeshima, Y. (2004). Neurogenin3 delineates the earliest stages of spermatogenesis in the
761 mouse testis. Developmental biology *269*, 447-458.
762 Yu, T., Fan, K., Ozata, D.M., Zhang, G., Fu, Y., Theurkauf, W.E., Zamore, P.D., and Weng, Z. (2021).
763 Long first exons and epigenetic marks distinguish conserved pachytene piRNA clusters from
764 other mammalian genes. Nature communications *12*, 73.
765 Zhang, Q., Ji, S.Y., Busayavalasa, K., and Yu, C. (2019). SPO16 binds SHOC1 to promote
766 homologous recombination and crossing-over in meiotic prophase I. Sci Adv *5*, eaau9780.
767 Zhang, Y., Liu, T., Meyer, C.A., Eeckhoute, J., Johnson, D.S., Bernstein, B.E., Nusbaum, C., Myers,
768 R.M., Brown, M., Li, W.*, et al.* (2008). Model-based analysis of ChIP-Seq (MACS). Genome biology
769 *9*, R137.
770 Zhao, B., Chen, Y., Jiang, N., Yang, L., Sun, S., Zhang, Y., Wen, Z., Ray, L., Liu, H., Hou, G.*, et al.*
771 (2019). Znhit1 controls intestinal stem cell maintenance by regulating H2A.Z incorporation.
772 Nature communications *10*, 1071.
773 Zheng, H., and Xie, W. (2019). The role of 3D genome organization in development and cell
774 differentiation. Nature reviews Molecular cell biology.
775 Zickler, D., and Kleckner, N. (2023). Meiosis: Dances Between Homologs. Annu Rev Genet.
776

777

Acknowledgments: We thank Chuan He for N3-kethoxal and Christopher L. Baker for meiotic chromatin state data. **Funding:** This work was supported by grants from the National Key Research and Development Program of China (2022YFA0806200, 2018YFC1003500, 2018YFA0800100, 2021YFC2501800), the National Natural Science Foundation of China (32192403, 81971443, 32300702, 32350710191), the Science and Technology Major Project of Inner Mongolia Autonomous Region of China to the State Key Laboratory of Reproductive Regulation and Breeding of Grassland Livestock (2020ZD0008). Shenfei Sun was supported by the fellowship of China Postdoctoral Science Foundation (2022M720797) and the Postdoctoral Fellowship Program (Grade B) of China Postdoctoral Science Foundation (GZB20230161).

Author Contributions: S.S. and X.L. conceived and designed the study; S.S. performed most of the experiments with the help of Y.J., Q.Z., H.P., F.H., X.Z., Y.G., X.Y., K.G., W.W., H.L., Z.S., Y.S., X.T., M.Y., and R.L.; Y.J. and N.J. performed the bioinformatics analysis; X.L. supervised the work and acquired the funding support; and S.S. and X.L. wrote the manuscript, with contributions from all authors. **Competing interests:** The authors declare that they have no competing interests. **Data and materials availability:** The NGS data generated in this study were deposited to the NCBI SRA database under accession numbers SRP467214 (RNA-seq and ChIP-seq data) and SRP467448 (ATAC-seq and KAS-seq data).

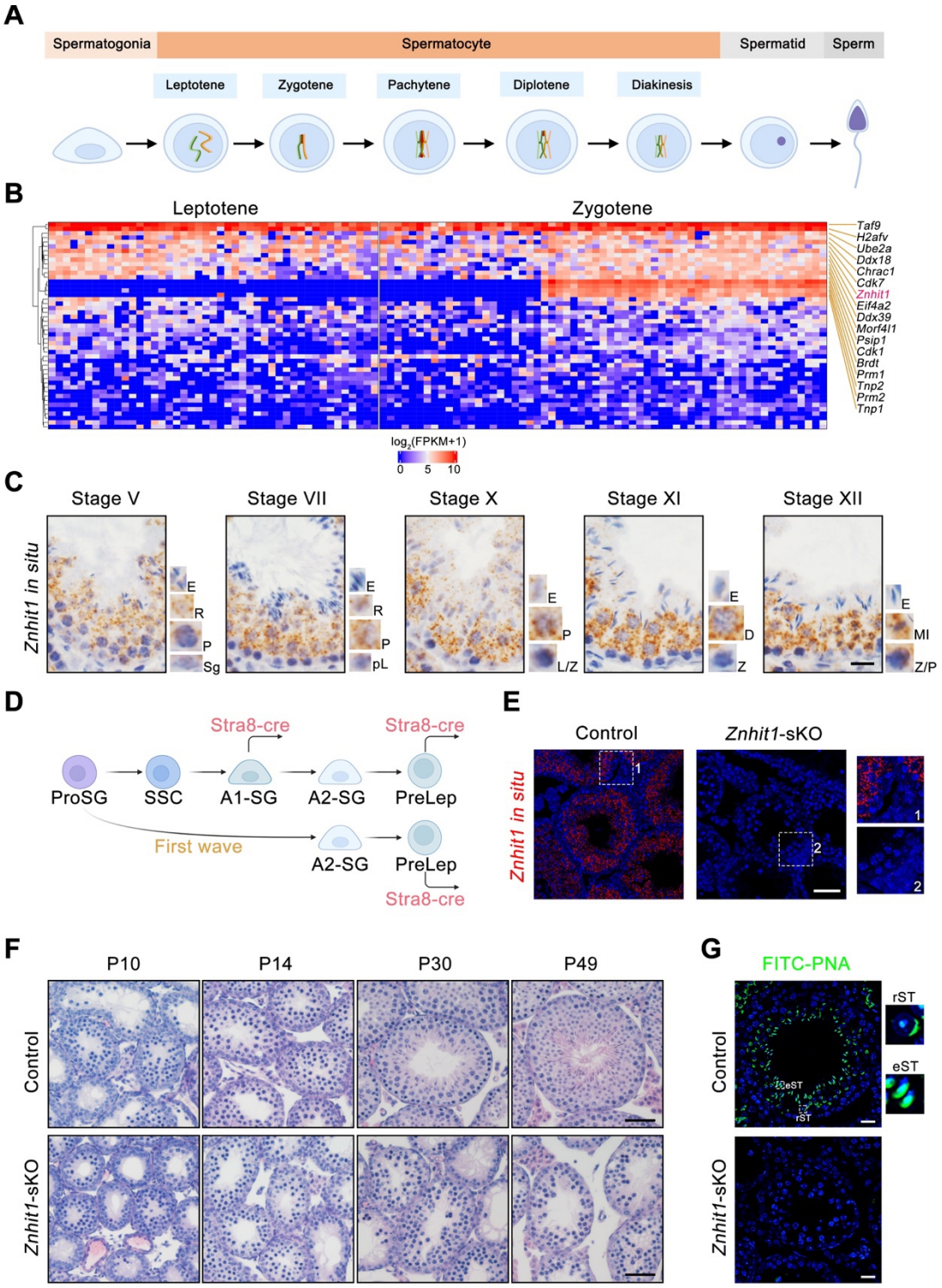

Figure 1 | Znhit1 deletion in spermatocytes disrupts spermatogenesis. (**A**) Schematic representation of the male germline development in mice. (**B**) Heatmap showing the clustering of 47 epigenetic factors based on the transcription levels in leptotene and zygotene spermatocytes. (**C**) *Znhit1* in situ hybridization in postnatal day 60 (P60) testis sections. Scale bar, 20 μm. Sg, spermatogonia; pL, preleptotene; L, leptotene; Z,

805 zygotene; P, pachytene; D, diplotene, MI, metaphase; R, round spermatids; E, elongating
806 spermatids. (**D**) Schematic diagram showing the onset of Stra8-cre expression in the male
807 germline development. (**E**) *Znhit1* in situ hybridization in P42 testis sections. Scale bar,
808 50 μm. (**F**) Histological testicular sections in control or *Znhit1*-sKO testis sections at the
809 indicated times. Scale bar, 50 μm. (**G**) Immunostaining of PNA in testis sections from
810 control or *Znhit1*-sKO mice at the indicated times. rST, round spermatids; eST, elongating
811 spermatids. Scale bar, 20 μm. All images are representative of n = 3 mice per genotype.
812

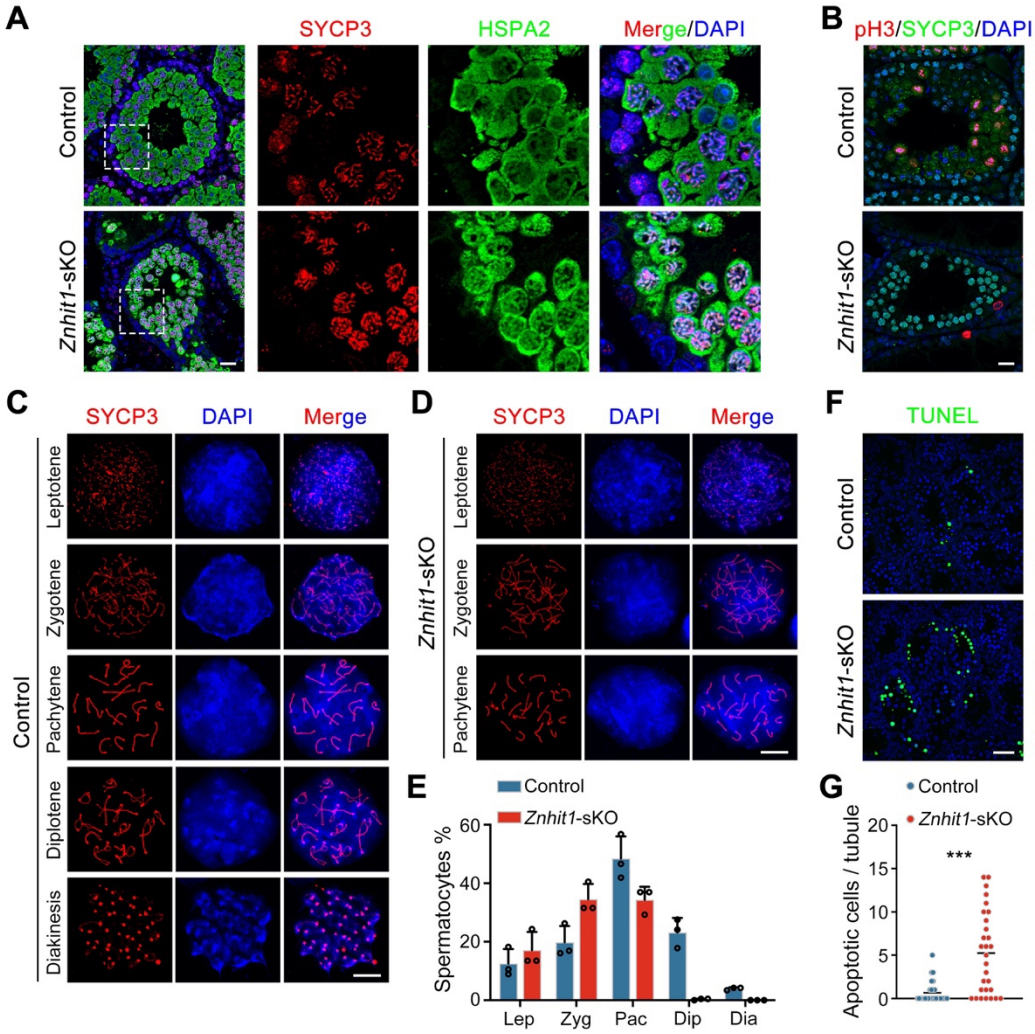

Figure 2 | Znhit1 deletion leads to meiotic pachytene arrest. (**A**) Immunostaining of SYCP3 and HSPA2 in testis sections of P35 control or *Znhit1*-sKO mice. Scale bar, 20 µm. (**B**) Immunostaining of SYCP3 and pH3 in testis sections of P35 control or *Znhit1*-sKO mice. Scale bar, 20 µm. (**C**-**E**) Immunostaining of SYCP3 in spermatocyte chromosome spreads of control (**C**) or *Znhit1*-sKO mice (**D**). Quantitative data are shown in (**E**). Scale bar, 10 µm. (**F** and **G**) TUNEL staining in testis sections from P14 control or *Znhit1*-CKO mice. Quantitative data are shown in (**G**). Scale bar, 40 µm. All images are representative of n = 3 mice per genotype. Data are presented as the mean ± s.d. *** $p < 0.001$.

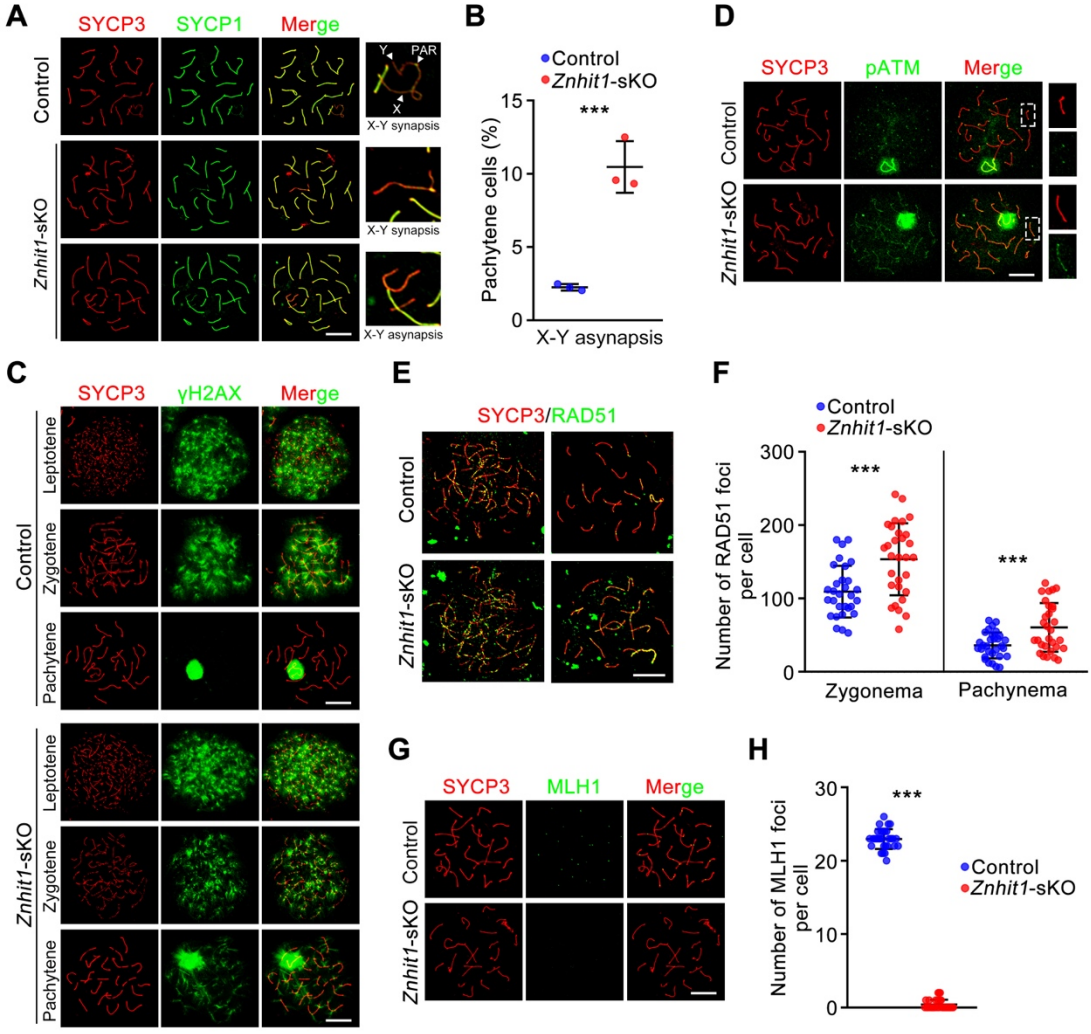

Figure 3 | Znhit1 controls meiotic recombination. (**A** and **B**) Immunostaining of SYCP3 and SYCP1 in spermatocyte chromosome spreads of control or *Znhit1*-sKO mice. X, X chromosome; Y, Y chromosome; PAR, pseudoautosomal region. Quantitative data are shown in (**B**). Scale bar, 10 μm. (**C**) Immunostaining of SYCP3 and γH2AX in spermatocyte chromosome spreads of control or *Znhit1*-sKO mice. Scale bar, 10 μm. (**D**) Immunostaining of SYCP3 and pATM in spermatocyte chromosome spreads of control or *Znhit1*-sKO mice. Scale bar, 10 μm. (**E** and **F**) Immunostaining of SYCP3 and RAD51 in spermatocyte chromosome spreads of control or *Znhit1*-sKO mice. Quantitative data are shown in (**F**). Scale bar, 10 μm. (**G** and **H**) Immunostaining of SYCP3 and MLH1 in spermatocyte chromosome spreads of control or *Znhit1*-sKO mice. Quantitative data are shown in (**H**). Scale bar, 10 μm. All images are representative of n = 3 mice per genotype. Data are presented as the mean ± s.d. *** $p < 0.001$.

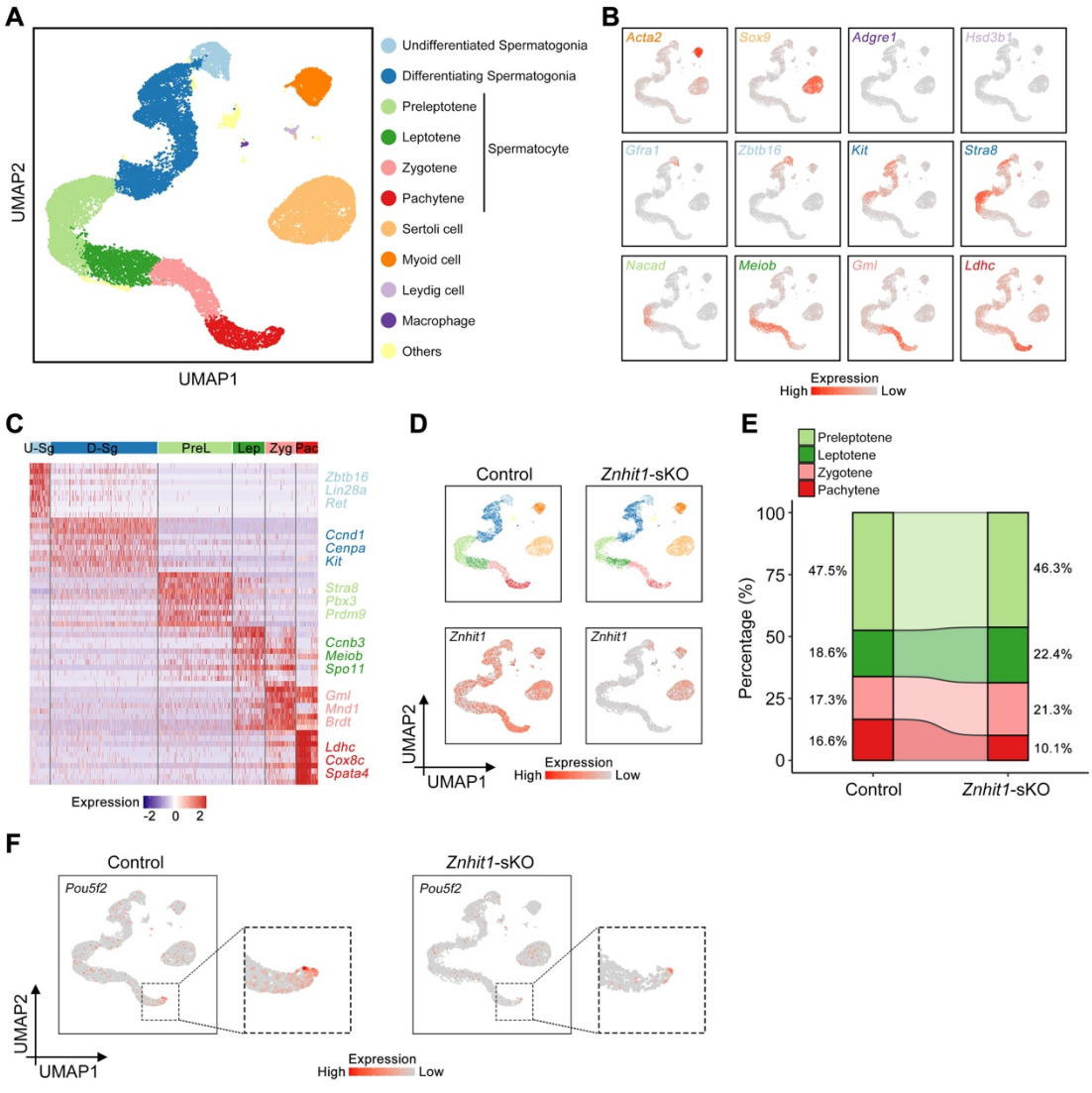

Figure 4 | Spermatocyte transcriptome analysis using scRNA-seq. (**A**) UMAP plot showing the annotated germ cells captured from both control and *Znhit1*-sKO testicular cells. (**B**) Expression of selected markers identifying major somatic cell types and germ cell types on the UMAP plot. UMAP plot showing the expression patterns of *Znhit1* in control or *Znhit1*-sKO testicular cells. (**C**) Heatmap showing the top marker genes of each cell cluster from scRNA-seq data. U-Sg, undifferentiated spermatogonia; D-Sg, differentiating spermatogonia; PreL, preleptotene; Lep, leptotene; Zyg, zygotene; Pac, pachytene. (**D**) Top: UMAP plot showing the annotated germ cells captured from control or *Znhit1*-sKO testicular cells. Down: UMAP plot showing the expression patterns of *Znhit1* in control or *Znhit1*-sKO testicular cells. (**E**) Bar plot showing the percentage of major spermatocyte types for control or *Znhit1*-sKO testicular cells. (**F**) UMAP plot

849 showing the expression patterns of *Pou5f2* in control or *Znhit1*-sKO germ cells.

850

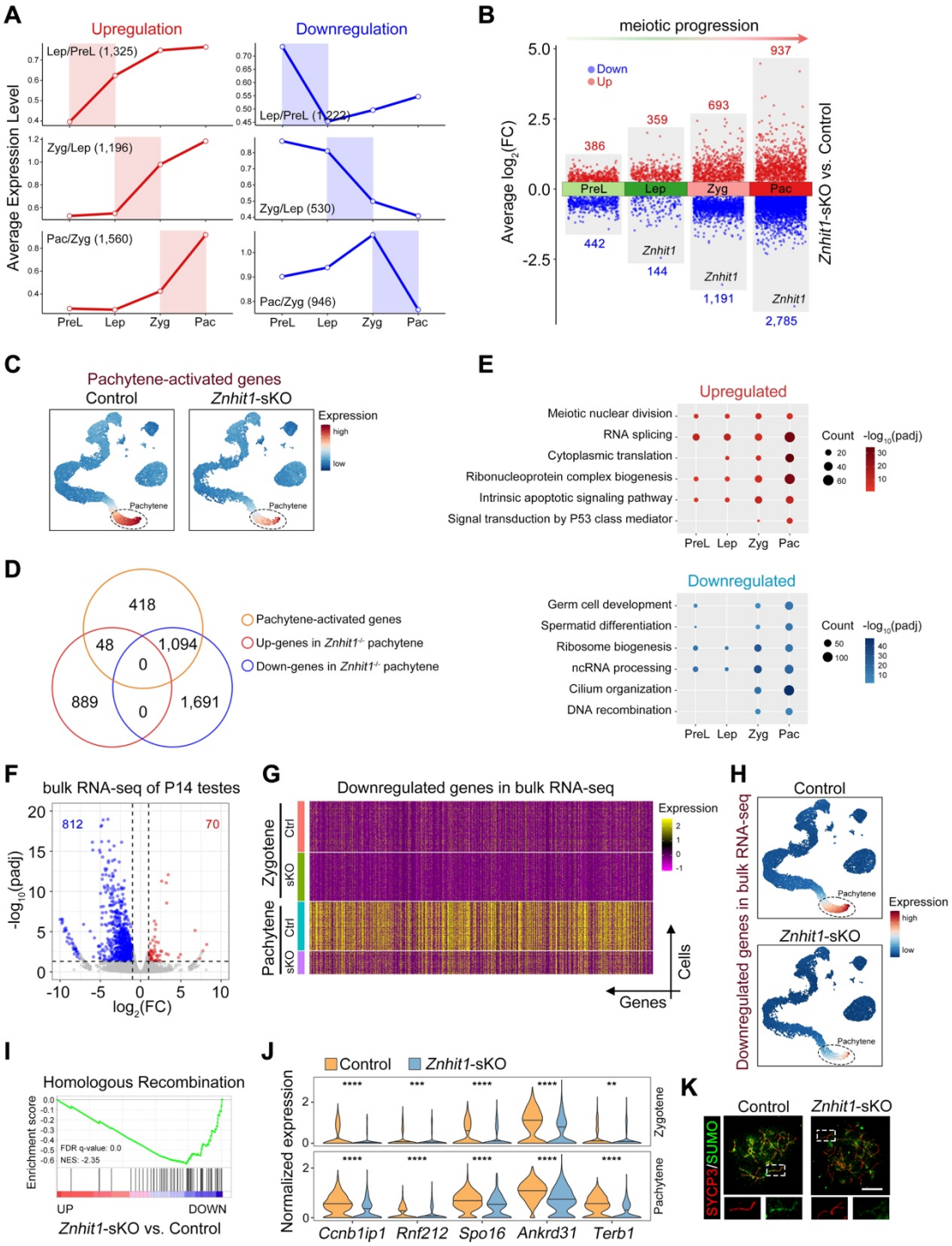

Figure 5 | Znhit1 deletion impairs meiotic transcriptional activation. (**A**) Line graph showing DEGs (upregulation or downregulation) in two consecutive spermatocyte stages. PreL, preleptotene; Lep, leptotene; Zyg, zygotene; Pac, pachytene. (**B**) Volcano plot showing the distribution of upregulated and downregulated DEGs for each cell type in spermatocytes between control or *Znhit1*-sKO testicular cells. (**C**) Cluster annotation on the basis of the expression of pachytene-activated genes in control or *Znhit1*-sKO

858 testicular cells. (**D**) Venn plots showing the number of shared genes between pachytene-
859 activated genes and DEGs in *Znhit1*-sKO pachytene spermatocytes. (**E**) Representative
860 shared Gene Ontology (GO) terms of upregulated (upper) and downregulated (lower)
861 DEGs at consecutive spermatocyte stages. (**F**) Volcano plot showing differentially
862 expressed genes (DEGs) in bulk RNA-seq following Znhit1 deletion (n = 2). (**G**)
863 Heatmap depicting the expression of the indicated genes at the zygotene and pachytene
864 stages in the scRNA-seq data. (**H**) Cluster annotation on the basis of the expression of
865 downregulated genes in bulk RNA-seq between control and *Znhit1*-sKO testicular cells.
866 (**I**) GSEA of RNA-seq data for the control and *Znhit1*-sKO testicular cells. Selected gene
867 sets encoded products related to homologous recombination. (**J**) Violin plots showing
868 downregulated DEGs of Znhit1-deficient zygotene cells and pachytene cells related to
869 homologous recombination. (**K**) Immunostaining of SYCP3 and SUMO2/3 in
870 spermatocyte chromosome spreads of control or *Znhit1*-sKO mice. Scale bar, 10 μm.
871 cluster genes. ** $p < 0.01$, *** $p < 0.001$, **** $p < 0.0001$.
872

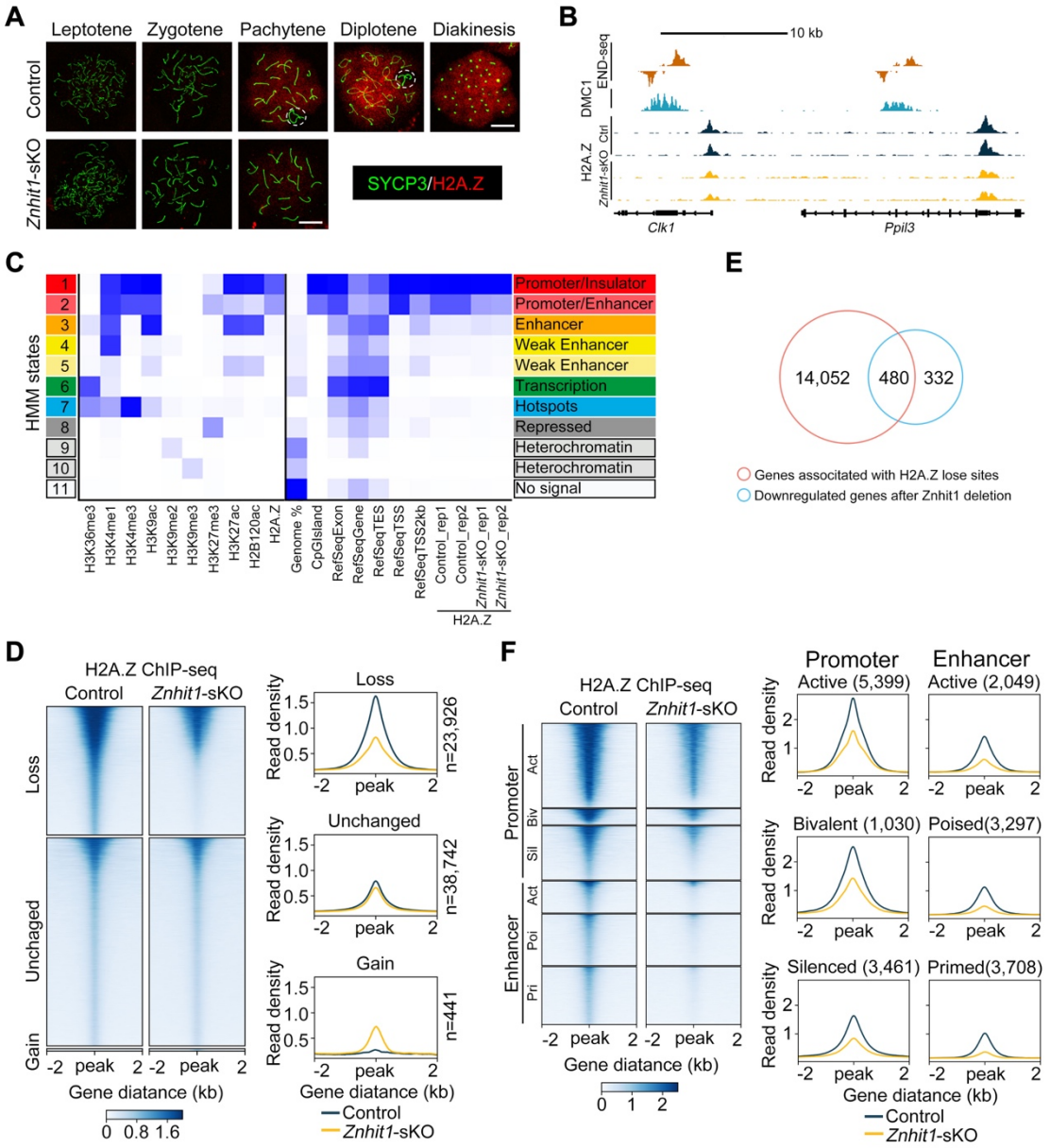

Figure 6 | Znhit1 regulates H2A.Z binding on promoter and enhancer regions. (**A**) Immunostaining of SYCP3 and H2A.Z in spermatocyte chromosome spreads of control or *Znhit1*-sKO mice. The dashed circle indicates X-Y chromosomes. Scale bar, 10 μm. (**B**) Representative tracks of END-seq, DMC1-SSDS, and H2A.Z ChIP-seq in wild-type, control, or *Znhit1*-sKO testicular cells. (**C**) Heatmaps of chromatin states produced by ChromHMM and showing different enrichment for H2A.Z in control or *Znhit1*-sKO testicular cells. (**D**) Heatmaps and mean plots of H2A.Z ChIP-seq signal in control or *Znhit1*-sKO testicular cells (n = 2). (**E**) Venn diagram showing the overlap between decreased H2A.Z-bound genes and downregulated genes in *Znhit1*-sKO testicular cells.

883 (**F**) Heatmaps and mean plots of downregulated H2A.Z ChIP-seq signals surrounding
884 different types of promoters and enhancers.
885

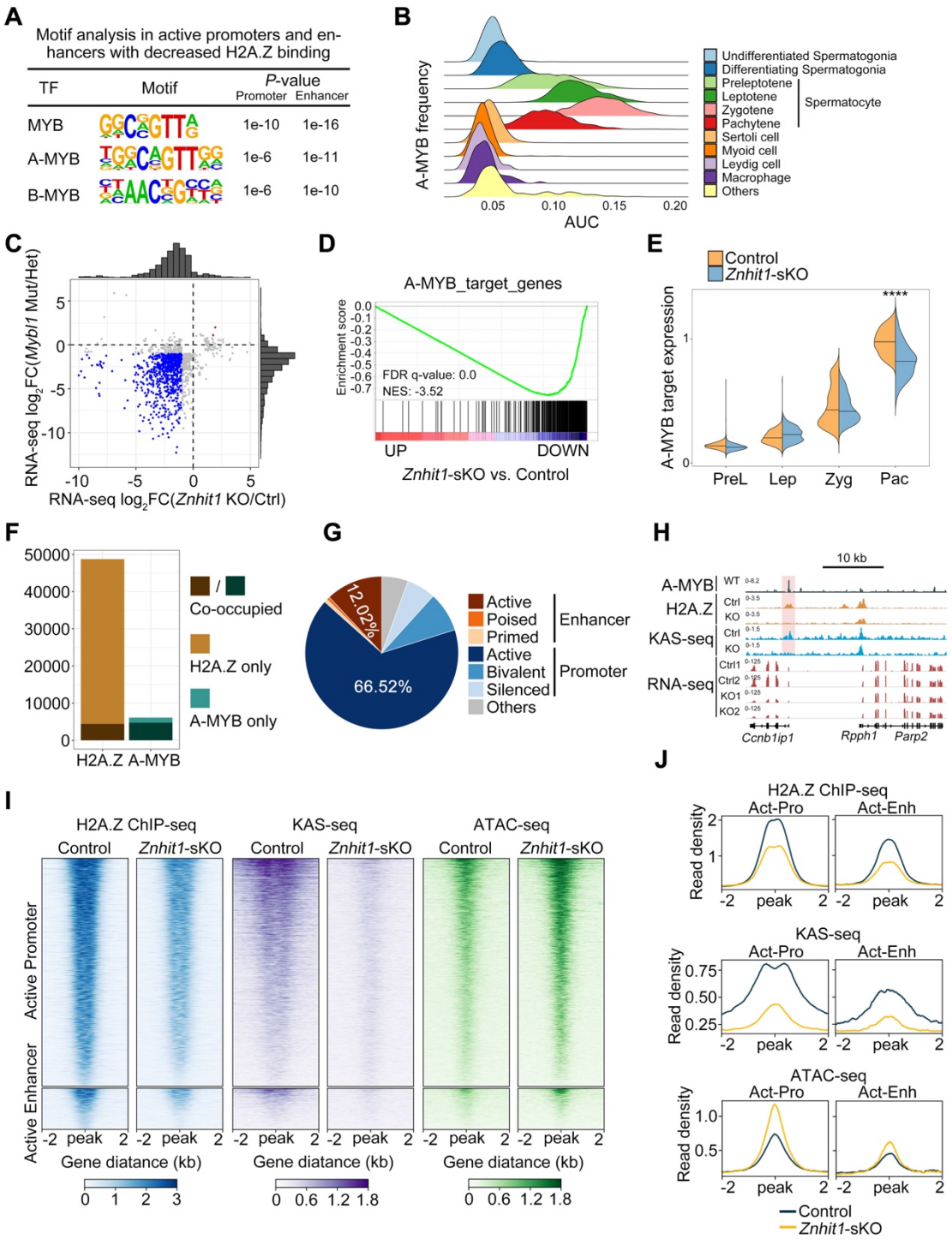

Figure 7 | Znhit1/H2A.Z/A-MYB axis regulates enhancer activation and gene expression. (**A**) Motif analysis of active promoters or active enhancers with decreased H2A.Z binding for putative transcription factor (TF)-binding sites using the HOMER database. (**B**) Ridge map showing the A-MYB activity (AUC) at each cell type. (**C**) Scatter plot with marginal histograms comparing the fold change of DEGs from A-MYB-related RNA-seq data with Znhit1-related RNA-seq data in P14 testicular cells. (**D**)

GSEA of RNA-seq data for the control and *Znhit1*-sKO testicular cells. Selected gene sets encoded products related to A-MYB target genes. (**E**) Violin plots showing the expression of A-MYB target genes at consecutive spermatocyte stages. (**F**) Histogram showing H2A.Z and A-MYB binding sites. (**G**) Pie chart showing the distribution of H2A.Z and A-MYB co-binding sites. (**H**) Representative H2A.Z ChIP-seq tracks, KAS-seq signals, and RNA-seq signals of the *Ccnb1ip1* locus in the control and *Znhit1*-sKO testicular cells, compared with A-MYB ChIP-seq peaks. (**I** and **J**) Heatmaps and mean plots of H2A.Z ChIP-seq, KAS-seq, and ATAC-seq showing signal changes within A-MYB and H2A.Z co-binding active promoters or active enhancers. **** $p < 0.0001$.

Supplementary Materials for

H2A.Z deposition at meiotic prophase I underlies homologous recombination and pachytene genome activation during male meiosis

Shenfei Sun *et al.*

*Corresponding author. Email: Xinhua Lin, xlin@fudan.edu.cn; Shenfei Sun shenfei_sun@fudan.edu.cn

This PDF file includes:

Figs. S1 to S9

Other Supplementary Material for this manuscript includes the following:

Tables. S1 to S8

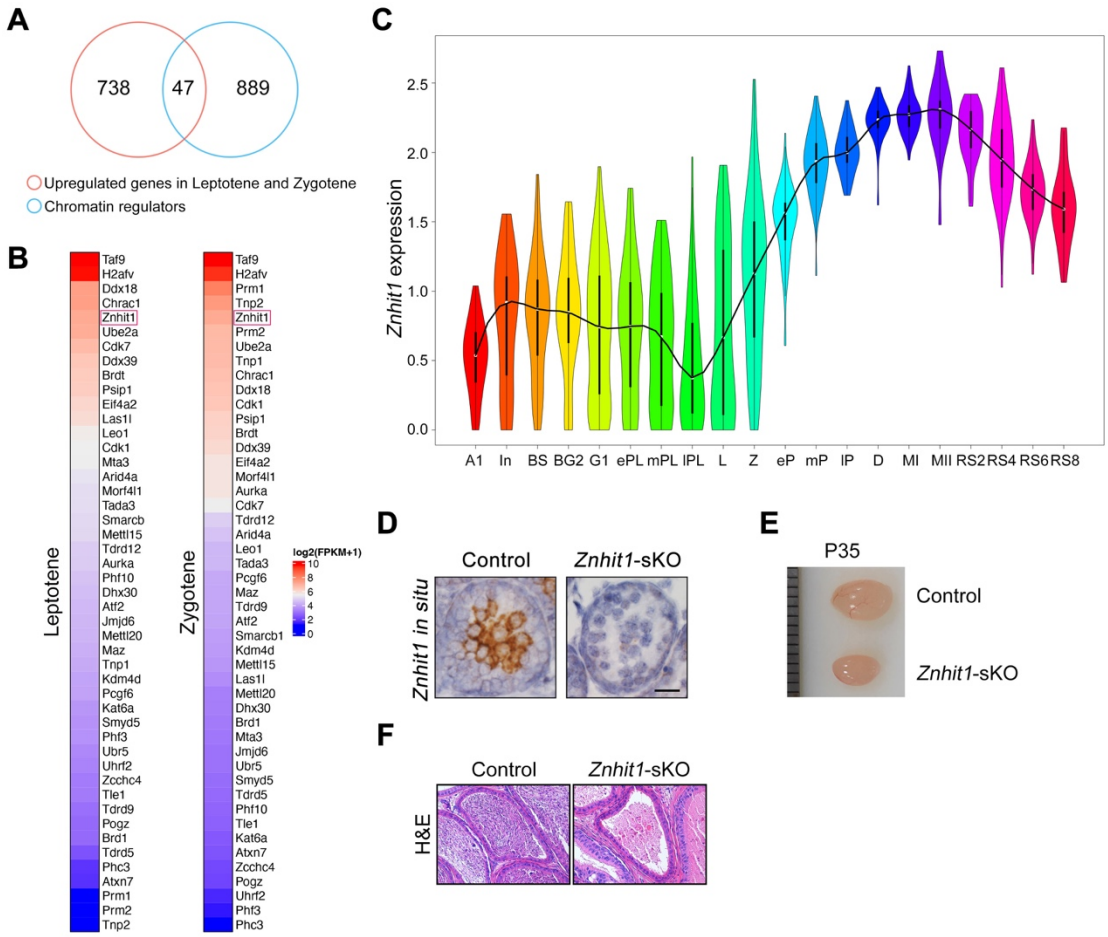

Figure S1. Znhit1 expression during meiotic progression and spermatocyte-specific deletion of Znhit1 with Stra8-cre. (**A** and **B**) Venn diagram and heatmaps showing chromatin regulators highly expressed during leptotene and zygotene spermatocytes. (**C**) Violin plot showing Znhit1 transcription level during spermatogenesis. Gene expression profiles derived from published data (Chen et al, 2018). (**D**) Znhit1 in situ hybridization in P14 testis sections. (**E**) Testis size comparison between control and Znhit1-sKO mice at P35. (**F**) Hematoxylin and eosin (H&E) - stained testis sections from control and Znhit1-sKO mice at P60.

943

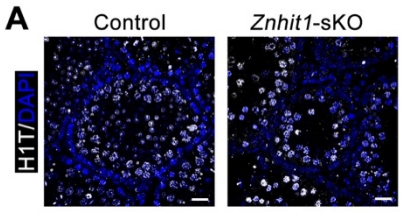

944 **Figure S2. H1T^{+} pachytene spermatocytes are detected in *Znhit1*-sKO testes.** (**A**)
945 Immunostaining of H1T in testis sections from control and *Znhit1*-sKO mice at P35.
946 Scale bar, 20 μm.
947

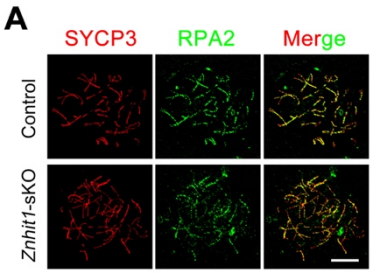

Figure S3. Znhit1 controls meiotic recombination. (**A**) Immunostaining of SYCP3 and RPA2 in spermatocyte chromosome spreads of control or *Znhit1*-sKO mice. Scale bar, 10 μm.

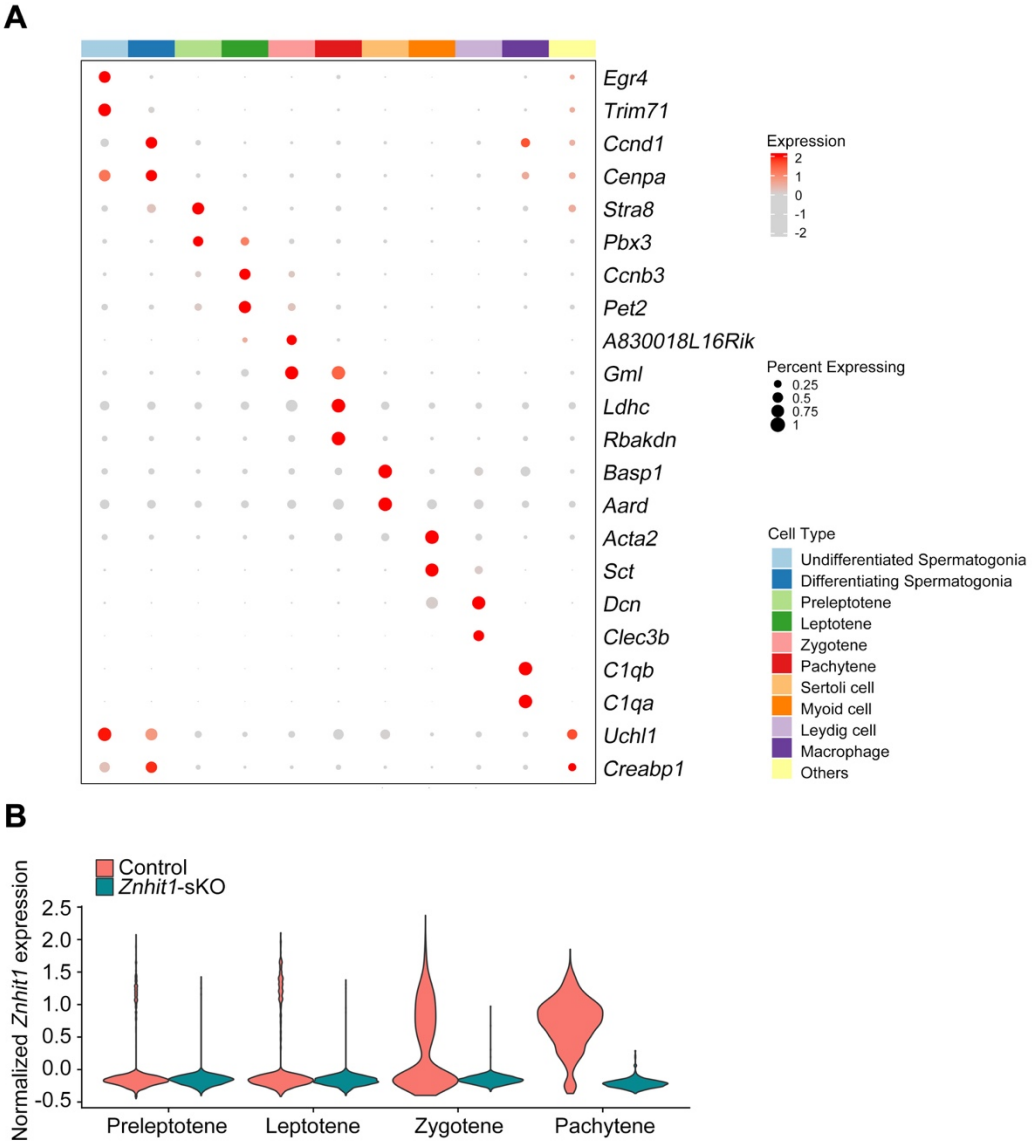

Figure S4. Single-cell RNA-seq of testicular cells. (**A**) Dot plot showing the relative expression and the percentage of cells expressing selected markers across scRNA-seq clusters. (**B**) Violin plot showing the normalized expression of *Znhit1* in control and *Znhit1*-sKO spermatocytes at consecutive stages.

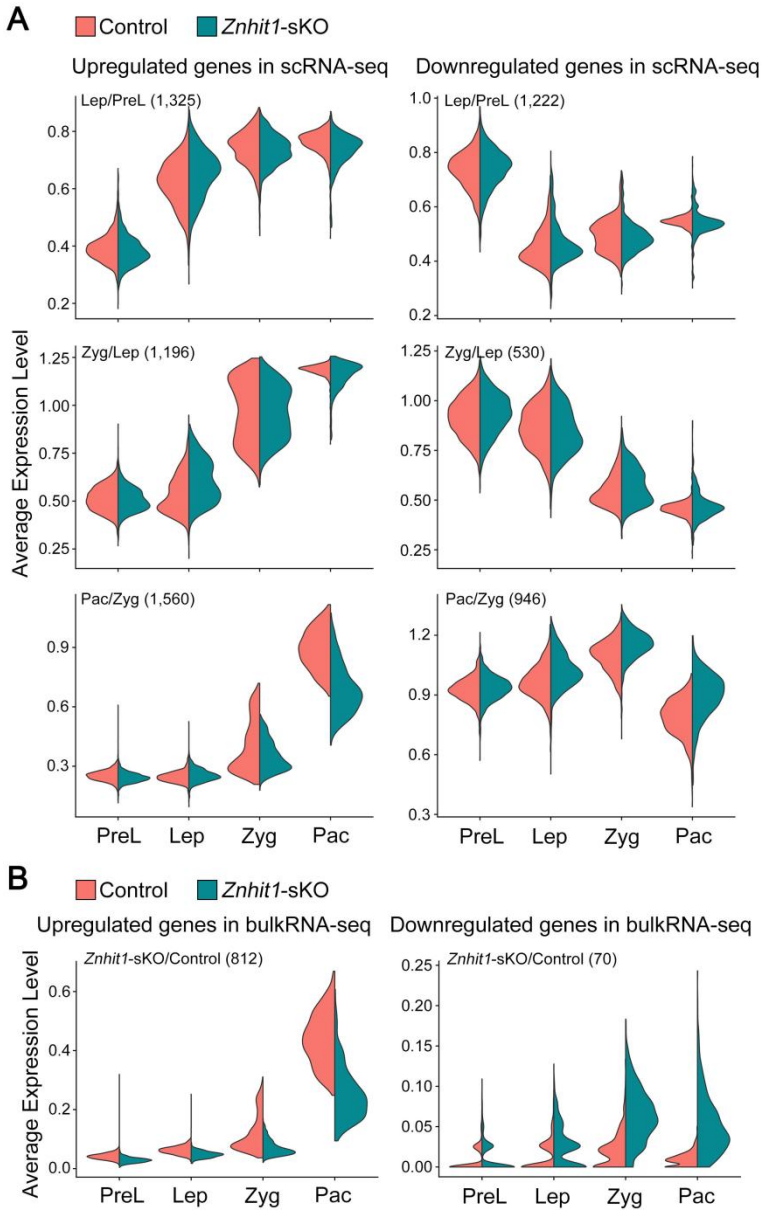

Figure S5. Single-cell transcriptomic analysis of meiotic genome activation. (**A**) Violin plots showing the average expression level of upregulated or downregulated genes between two consecutive spermatocyte stages. (**B**) Violin plots showing the average expression level of upregulated or downregulated genes between P14 control and *Znhit*1-sKO testicular cells. PreL, preleptotene; Lep, leptotene; Zyg, zygotene; Pac, pachytene.

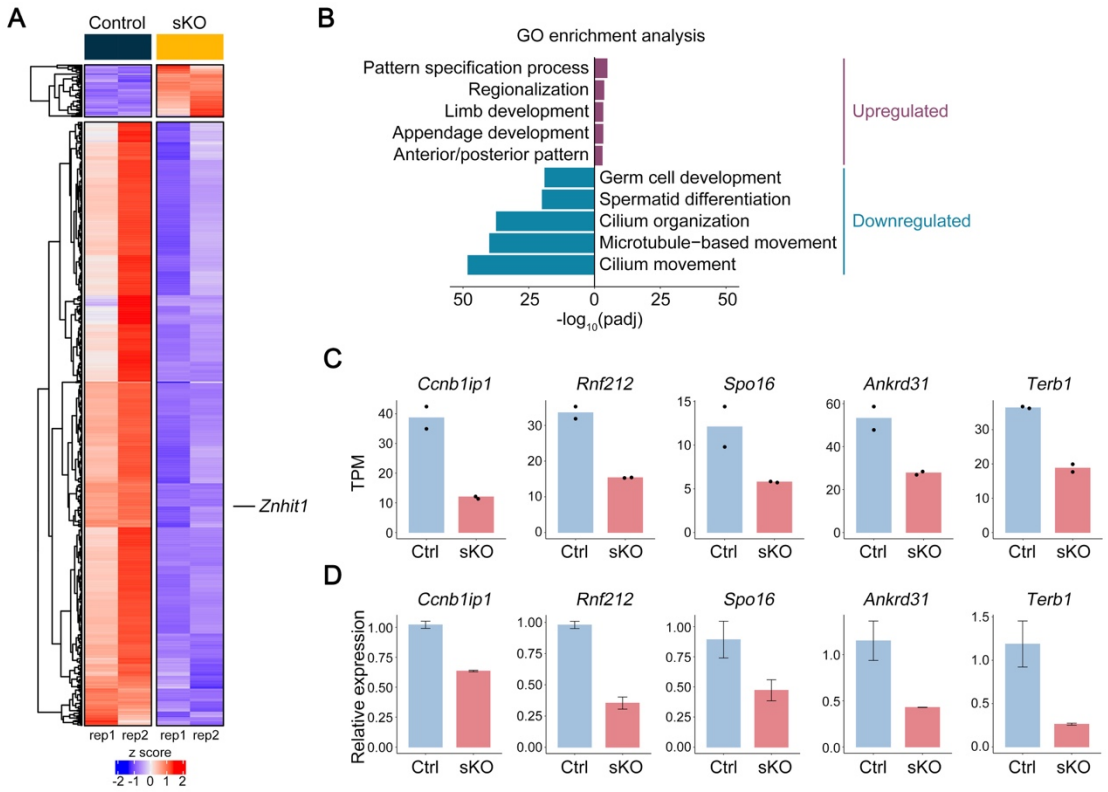

Figure S6. differentially expressed genes (DEGs) in P14 testicular cells between control and Znhit1-sKO mice. (**B**) Gene ontology (GO) analysis of DEGs showing changed biological processes. (**C** and **D**) Bar charts showing HR-related gene expression in P14 control and *Znhit*1-sKO testes. Data from bulk RNA-seq are shown in (**C**). Validated data from RT-qPCR are shown in (**D**). Ctrl, control; sKO, *Znhit1*-sKO.

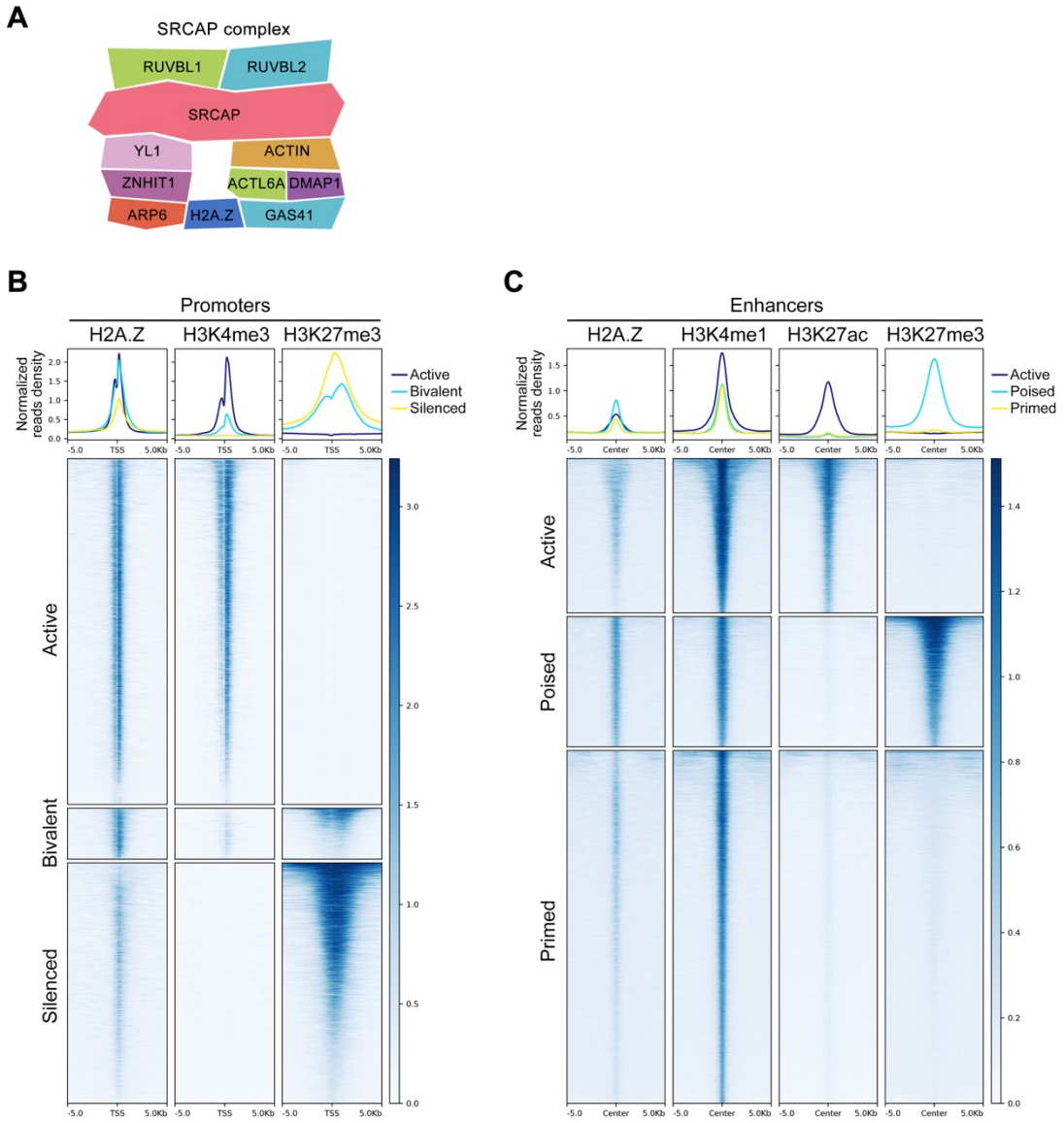

977

978 **Figure S7. H2A.Z is enriched at meiotic gene promoters and enhancers.** (**A**)
979 Schematic representation of the components of the SRCAP chromatin remodeling
980 complex. (**B**) Heatmaps showing H2A.Z ChIP-seq signals surrounding different types of
981 promoters. (**C**) Heatmaps showing H2A.Z ChIP-seq signals surrounding different types of
982 enhancers.

983
984

985

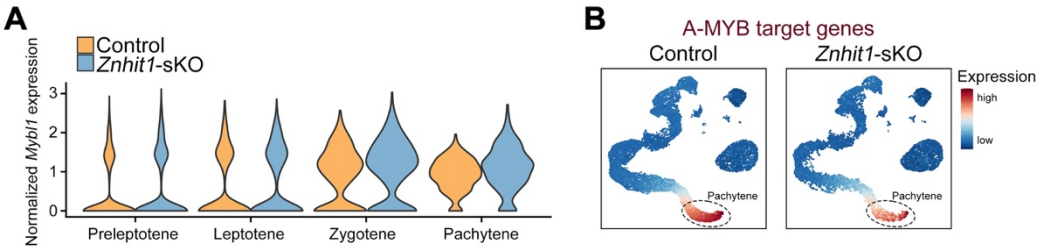

986 **Figure S8. Znhit1 deletion downregulates the expression of A-MYB target genes.** (**A**)
987 Violin plot showing the normalized expression of *Mybl1* in control and *Znhit1*-sKO
988 spermatocytes at consecutive stages. (B) Cluster annotation on the basis of the expression
989 of A-MYB target genes in control or *Znhit1*-sKO testicular cells.

990
991

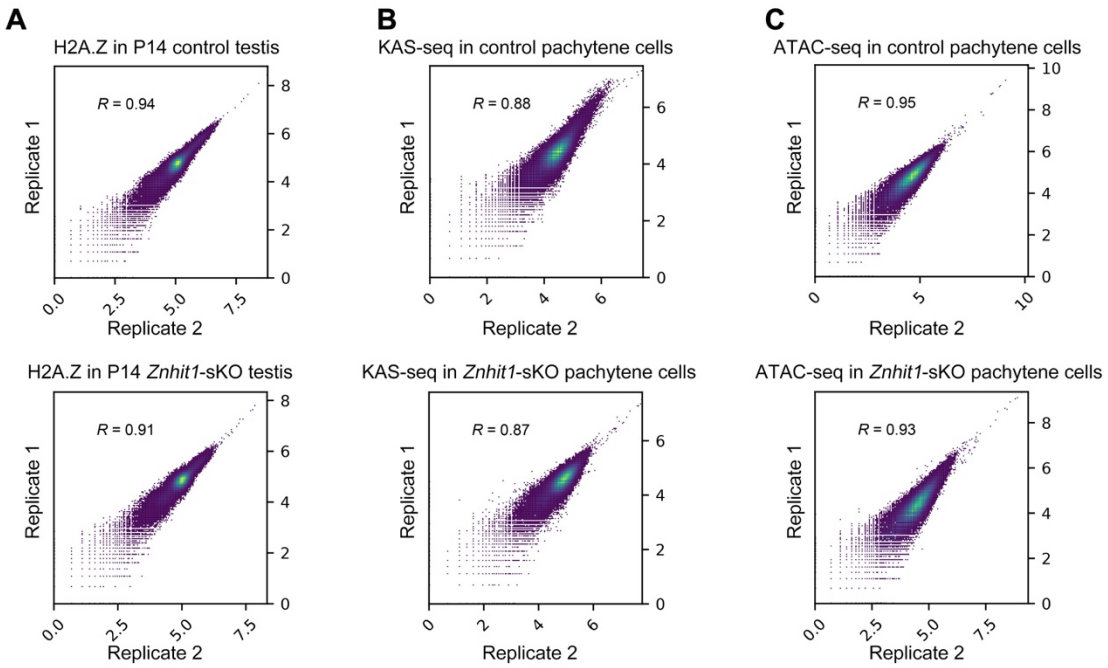

992

993 **Figure S9. Reproducibility of replicates in this study.** (**A**) Scatter plots showing H2A.Z
994 enrichments in P14 control or *Znhit1*-sKO testes for two independent H2A.Z ChIP-seq
995 replicates. Pearson correlation coefficients are indicated. (**B**) Scatter plots showing KAS-
996 seq signals in P14 control or *Znhit1*-sKO pachytene cells for two independent H2A.Z
997 ChIP-seq replicates. Pearson correlation coefficients are indicated. (**C**) Scatter plots
998 showing ATAC-seq signals in P14 control or *Znhit1*-sKO pachytene cells for two
999 independent H2A.Z ChIP-seq replicates. Pearson correlation coefficients are indicated.

1000
1001

1002